Politecnico di Torino

Master's Degree in Energy and Nuclear Engineering

Master's Degree Thesis

Predictive modelling of the transport of impurities emitted from a liquid metal divertor in the core of the EU-DEMO future fusion reactor

Supervisors	Candidate
Prof. Fabio SUBBA	Elisabetta BRAY
Prof. Giuseppe Francesco NALLO	
Dott. Chiara MARCHETTO	
Dott. Teobaldo LUDA DI CORTEMIGLIA	

July 2023

Abstract

The aim of this thesis is the development of an integrated model for the transport of impurities ejected from the surface of a liquid metal divertor (LMD) inside the core plasma of the European DEMO (EU-DEMO) future fusion reactor. Nuclear fusion is a promising energy production system based on the process that lights up the stars, and the great challenge is to reproduce suitable conditions for fusion reactions to occur on Earth. The magnetic confinement approach, realized in machines called Tokamaks, consists in confining the fusion fuel - a plasma heated up to $\sim$ 100 million Celsius degrees - through a system of magnets. One of the key challenges to be solved is represented by the interactions between plasma and wall materials, where a fraction of the total power must be exhausted. This role is fulfilled by the divertor, where most of the heat and particles are directed and where very effective cooling mechanisms are employed. In view of the significantly larger amount of power produced by EU-DEMO (the first tokamak planned to produce electricity that was chosen as the reference system for this work) with respect to present-day experiments, the implementation of a self-healing liquid metal divertor, unlike traditional solid one, has been considered. This solution can exploit the evaporation process resulting from the hot plasma impacting its surface, leading to the formation of a cloud of particles in front of the divertor plates, which contribute to exhausting the incoming power via radiation processes. However, should the impurities evaporated from the wall reach the core plasma, the resulting pollution could contaminate it to the point that the fusion process is hindered. Studying the transport of these particles which can cause the plasma shutdown, throughout the Scrape Off Layer (SOL) - a thin region surrounding the reacting fusion plasma core - and the core itself, is necessary to assess the feasibility of the liquid metal divertor option, thus representing a strong motivation for this thesis, which can be regarded as a first step towards an integrated divertor-SOL-core model. As the initial phase of the work, transport phenomena due to classical, neoclassical, and turbulent effects have been thoroughly reviewed, to study the motion of impurities inside core plasma. Afterward, a comparison between Lithium and Tin (the most promising materials for a liquid metal divertor) in terms of their impact on the core plasma power balance has been performed. This required the study of their radial density distribution in the core plasma, identifying possible phenomena leading to undesired accumulation. This calculation has been performed using the ASTRA code, capable of solving the transport equation of background plasma and impurities. Neoclassical and turbulent effects have been considered in evaluating transport coefficients by means of NCLASS and TGLF codes, eventually leading to the calculation of the radial profiles of impurities and the correspondent radiated power. After having validated some preliminary results against shots from ASDEX-Upgrade, simulations for the EU-DEMO scenario have been prepared, both for the case of Lithium and Tin. Preliminary results depict the feasibility of using LMD for the reference scenario, employing checking to remain below specific fractional limits of impurity abundance, both for Lithium and Tin. In particular, Tin seems to be the best candidate, thanks to its capability of radiating very much even if in very low concentrations. This avoids the dilution of plasma, differently from the Lithium case, which decreases the main ions' concentration even if it is present in a very low fraction.

Acknowledgments

The work carried out in this thesis would not have been possible without the invaluable help of my supervisors who accompanied me in its development. Also inestimable was the help I received from *Daniel Fajardo, Clemente Angioni*, and *Emiliano Fable* who, with their enormous kindness, guided me in the development of the necessary skills for the use of the codes and in the understanding of the physics behind.

Table of Contents

1 Introduction 1
- 1.1 Fusion power production 1
- 1.2 Magnetic confinement in Tokamaks 2
- 1.3 The European roadmap towards the realization of fusion energy 5

2 Motivations of the work 8
- 2.1 The power exhaust problem in Tokamaks 8
- 2.2 Atomic processes at the plasma edge and role of the divertor 10
- 2.3 Liquid Metal Divertors 11

3 Transport in Tokamaks 15
- 3.1 Classical transport 16
- 3.2 Neoclassical transport 18
  - 3.2.1 Banana regime 19
  - 3.2.2 Plateau regime 20
  - 3.2.3 Pfirsch-Schluter regime 21
- 3.3 Turbulent transport 21
  - 3.3.1 ITG and ETG mechanism 22
  - 3.3.2 Trapped electron mode (TEM) 23
- 3.4 Impurities behavior 24

4 Core transport modelling 29
- 4.1 The ASTRA code 29
  - 4.1.1 The STRAHL code 32
  - 4.1.2 TGLF and NCLASS codes 33
- 4.2 Coupling strategy with SOLPS-ITER code 34

5 Setup of simulations and results 37
- 5.1 Setup of the simulations 37
- 5.2 Results 44
  - 5.2.1 Reference scenario without impurities 45

5.2.2 Lithium 47
5.2.3 Tin 54
5.2.4 Comparison between Lithium and Tin 62

6 Conclusions and future work 65

A Formulas for radiated power of Lithium and Tin 67
A.1 Lithium 67
A.2 Tin 68

Bibliography 71

Chapter 1

Introduction

1.1 Fusion power production

Fusion power production is one of the biggest challenges of the last decades, promising to generate electricity in a nearly inexhaustible, clean, and safe way by exploiting the physical process that lights up the stars.

Environmental issues that arose in recent years have led to the increasing demand for sustainable energy production, to avoid the usage of fossil fuels while providing energy for a wider market. Fusion energy is definitely suited for these purposes, helping also to have a much larger abundance and fairer distribution of resources. In fact, fusion power production is based on the nuclear fusion reaction between two isotopes of hydrogen, namely deuterium and tritium, that colliding are able to transform part of their mass into energy (17.6 MeV), proportionally split between the reaction products, namely a Helium nucleus (alpha particle) and an energetic neutron. The energy required to obtain a sufficient fusion reaction rate is such to maintain the reactant in the fourth state of matter: the plasma. This is made by fully ionized particles of fuel (deuterium and tritium), that reacting yield the above-mentioned alpha particles and highly energetic neutrons. Due to the momentum conservation principle, the latter takes the majority of the released energy [1]. Alpha particles are the ones that ensure the self-sustaining of the plasma, colliding with ions and electrons and exchanging thermal energy by friction, maintaining hot the system. Neutrons instead are the carriers of the kinetic energy that will be transformed into thermal one, before finally producing electricity.

The main problem that arises when the very hot plasma is generated is the capability of confining it without melting any surface it could encounter. To this end, the plasma must be controlled in a prescribed region, trying to avoid contact with any materials, while the condition to maintain it switched on has to be fulfilled. This last requirement is described by the *Lawson criterion*, reported in 1.1 :

$$n \cdot \tau_E \cdot T \geq 3 \cdot 10^{21}\ keV\ s/m^3 \tag{1.1}$$

Here n represents the plasma density, τ_E the *confinement time*, which simply describes the time for which particles are confined within the plasma, and T is the temperature of the plasma. From this equation, we understand that there are two ways to meet the requirement: either having a high confinement time and a relatively low density, or the opposite. The former case is exploited in the magnetic confinement concept, where a low-density plasma is confined by means of a complex system of magnets, while the latter is operated in inertial confinement, where a solid fuel pellet is ablated by a system of lasers.
In the framework of this thesis, magnetic confinement will be deeper studied, being the one on which Tokamaks' functioning is funded.

1.2 Magnetic confinement in Tokamaks

The concept behind the structure of Tokamaks is the idea of exploiting the charged nature of particles that compose the plasma through a complex system of magnetic fields which leads them to follow a closed trajectory. A deeper focus on the motion of particles inside a magnetized plasma will be done in chapter 3, but for the moment the general structure of the magnetic systems will be presented.

From figure 1.1, it is possible to distinguish three different magnetic systems, namely the toroidal field coils, the poloidal field coils, and the central solenoid. The *toroidal field magnet system* is composed of D-shaped magnets that completely surround the structure, giving the characteristic donut shape to the entire machine. A current is driven inside them and consequently, a magnetic field is generated in the toroidal direction. The toroidal magnetic field lines are then followed by the particles that however are easily lost by the radially decreasing strength of the field and could reach the wall. Moreover, the *poloidal magnetic field coil system* is added: it is made up of almost circular magnets located on the top and on the bottom of the reactor, and, driven by a current, a magnetic field in the poloidal direction is generated. These magnets are mainly used to shape the plasma for different purposes, while the last system is the *central solenoid*, which, exploiting the principle of the transformer, generates a vertical magnetic field that induces a toroidal current (*the plasma current*) inside the torus and a consequent poloidal magnetic field which has the role of preserving the equilibrium of the plasma itself. The combination of these systems is able to generate the helical trajectory of particles moving inside a tokamak which is shown in figure 1.1.

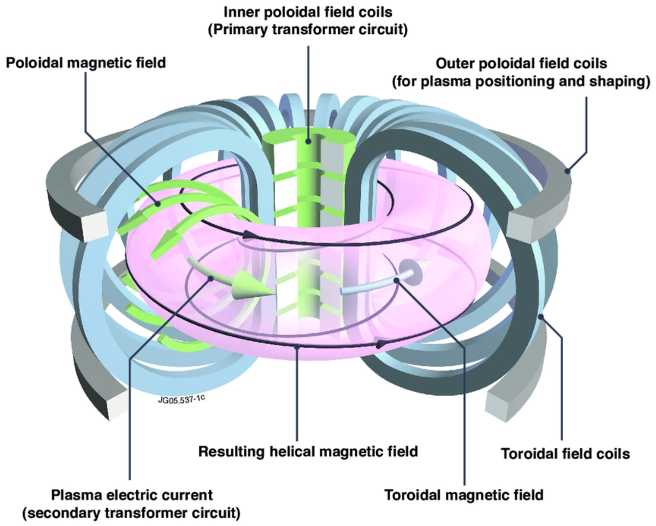

Figure 1.1: Representation of the system of magnets of a Tokamak and the consequent helical trajectory of a plasma particle. [2]

As previously stated, all the specific phenomena that lead to generating the resulting trajectory will be better explained in chapter 3. However, before delving deeper into the matter, it is important to understand how to exploit the confined plasma to produce energy.
The operating principle of Tokamaks is composed of a revolutionary concept, that is the fuel used - hydrogen isotopes - and the way energy is released - nuclear fusion - while the way in which electricity is actually produced relies on traditional technologies. Indeed, the neutrons that are produced by the fusion reaction impact the wall of the reactor, which is engineered such that their kinetic energy is converted to heat and extracted by a cooling circuit. This is finally connected to a turbine and generates electricity by the simplest means used in any kind of traditional power plant. Of course, the implementation of this technology is anything but trivial, and there are several components of Tokamaks that have been designed from scratch exactly for that specific purpose and that can be classified among the highest achievements of engineering and technology that scientific research has been able to produce so far.

The main components can be summarized by quoting the *magnets*, the *divertor*, and the *breeding blanket*. For what concerns magnets, besides the complexity of their structure, they have also the task of producing very high magnetic fields, of the order of 12 T (200 thousand times the terrestrial magnetic field), which means being traversed by a current of the order of 70-80 kA [3]. In the past, normal conductors were employed, but in recent years, in new experimental reactors *superconducting magnets* are used, to increase the efficiency. In fact, they are able to get zero electric resistance when cooled down to cryogenic temperatures. This implies the presence of a cryogenic system to maintain these extremely low temperatures. In this respect, it is instructive to notice the impressive temperature difference between the core plasma, at 100 thousand Celsius degrees, and the magnets, at cryogenic temperatures, just a few meters away.

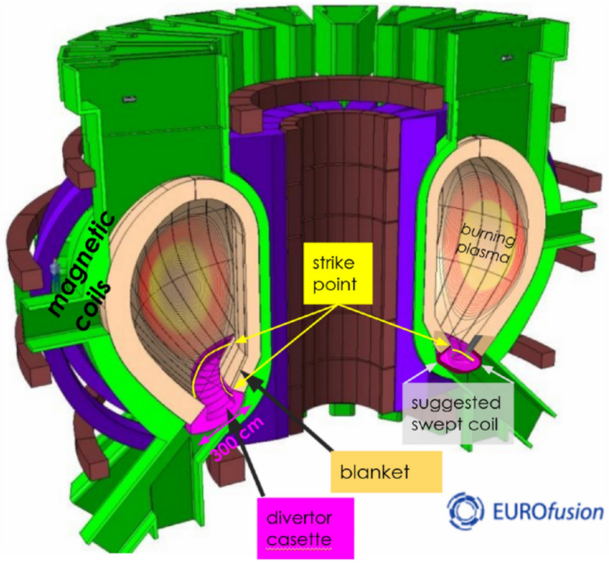

Figure 1.2: Picture of the main components of a Tokamak, namely the magnetic system, the blanket, and the divertor. [4]

The other two components are then devoted to handling, respectively, the problem of exhausting the power of the plasma when it necessarily touches the inner walls of the reactor, and the effective production of energy. On the *divertor*, most of the particles and heat fluxes are directed, thanks to the shaping of plasma by means of magnetic fields, and it extends toroidally throughout the entire bottom surface of the Tokamak. Finally, the *blanket* has to fulfill two main duties: the *Tritium breeding* - the continuous replenishment of tritium, exploiting the reaction between neutrons and Lithium - and the extraction of energy. To do so, the presence of both a breeder and a coolant is required. Currently, there are at least two different configurations proposed for this component, differing in the fluid that has to accomplish the cooling (water or helium), the breeder technologies, and varying also the structure of the system to better tackle the two tasks mentioned. They are the Water Cooled Lithium Led (WCLL) [5] and the Helium cooled Peeble Bed (HCPC) [6].

1.3 The European roadmap towards the realization of fusion energy

The goal of achieving energy production via fusion reactions appears closer today thanks to experimental reactors that have been built and operated all over the world from the early 50s up to the present day [7]. Europe has always been at the forefront of fusion development, thanks to the contribution of experimental reactors like JET (Joint European Torus) at the CCFE center in Oxford, ASDEX-Upgrade in Germany, and several others, exploring the most complex challenges of magnetic confinement, plasma physics, and engineering components.

Europe has developed a roadmap [8] that aims to demonstrate the commercial feasibility of fusion to produce electric energy and the EUROFusion, the European Consortium for the Development of Fusion Energy, was born in 2014 on the roots of older European agreements like EFDA (European Fusion Development Agreement), to join together European countries with this ambitious final goal. The roadmap starts taking the results obtained by the existing reactors all over the world and is divided into three main stages, in which ITER and DEMO reactors are the protagonists.

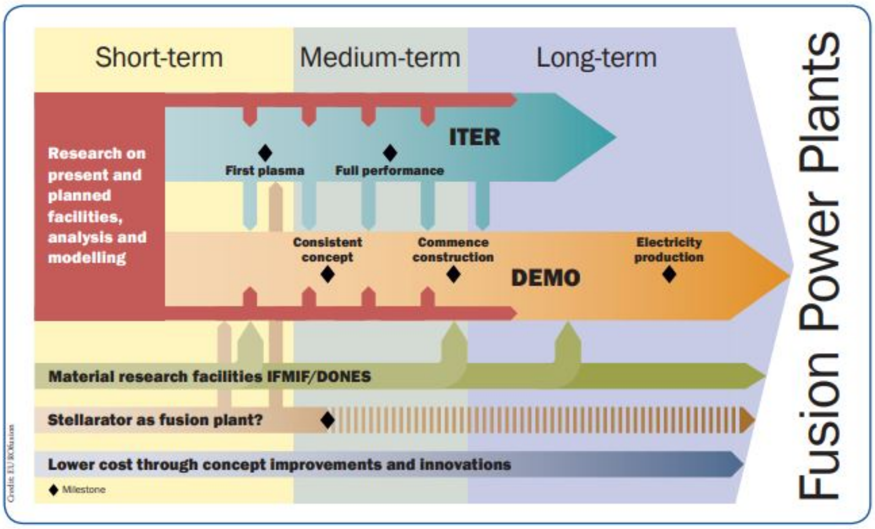

Figure 1.3: EUROfusion roadmap for the future perspective of nuclear fusion power plants. [8]

In the short term, the construction of ITER is planned together with its first shot of plasma in 2027, taking advantage of research from existing experiments like JET with its unique milestones obtained during years of operations (such as the

Deuterium-Tritium plasma) and other testing facilities. In the same period, which includes current days, the conceptual design of EU-DEMO (DEMOnstration Power Plant) is proceeding. In the medium term, ITER is supposed to be fully operational and the results of its experiments should give important improvements for the Engineering Desing phase of the EU-DEMO. Finally, in the long term perspective, ITER should achieve high performances and advanced technologies, so that the EU-DEMO design can be finalized and constructed in order to demonstrate the real capability of generating electricity from a fusion power plant, potentially around 2050-2060.

The biggest aim of this plan is the production of more energy than the one that is injected inside the system to generate and maintain the plasma, possibly reaching a completely self-sustained thermonuclear reaction - the so-called *ignition* condition. ITER [9] is supposed to demonstrate the capability of sustaining a plasma with a Q factor (the ratio between the power produced and the one given to the system) at least equal to 10. Nowadays the record is set to 1.5 achieved by National Ignition Facility at the Lawrence Livermore National Laboratory in California [10], an inertial confinement experiment, whereas the record for magnetic fusion belongs to JET and is 0.67, so it can be understood how bold is this goal. One way in which it will be possible to reach this and further milestones like the production of electric energy is by building reactors always bigger following a scaling law that connects the inner volume of plasma and the fusion power produced, with an increasing radius of plasma, as can be seen by the figure 1.4.

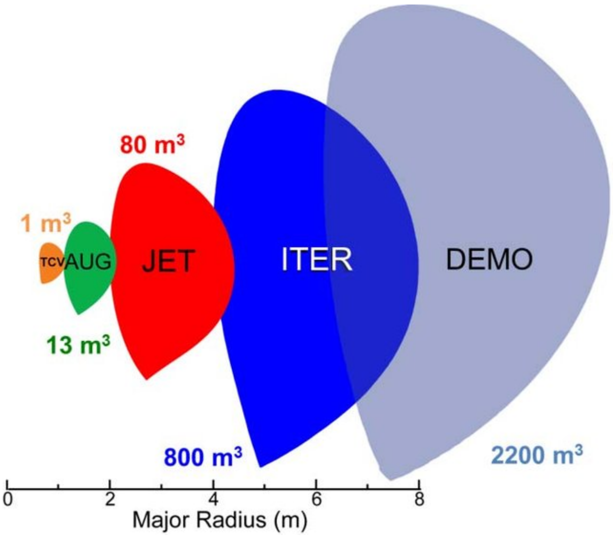

Figure 1.4: Evolution of plasma dimensions in the most important reactors existing and of future development like ITER and DEMO. [11]

Among the other possible solutions, it is worth quoting the case of the ARC (Affordable, Robust, Compact) project and the *stellarators*.
The former, currently under study at MIT which is building a test facility called SPARC (as Soon as Possible ARC) [12], employs High-Temperature Superconductor (HTS) rather than LTS as in ITER. This will allow to get the same confinement in a smaller volume.
The latter solution of the stellarator instead, consists of a complex system of magnets that are able to confine particles in a toroidal configuration without the need of inducing a plasma current, avoiding the usage of the central solenoid and so able to produce a continuos current and not pulsed like in the case of Tokamaks. The shape of these magnets is specifically tailored for the scope and makes the structure no more axisymmetric. The most famous stellarator is *Wendelstein 7-X* [13] located at the IPP research center in Greifswald-Germany, but also some brand-new start-ups are investing in this technology [14].

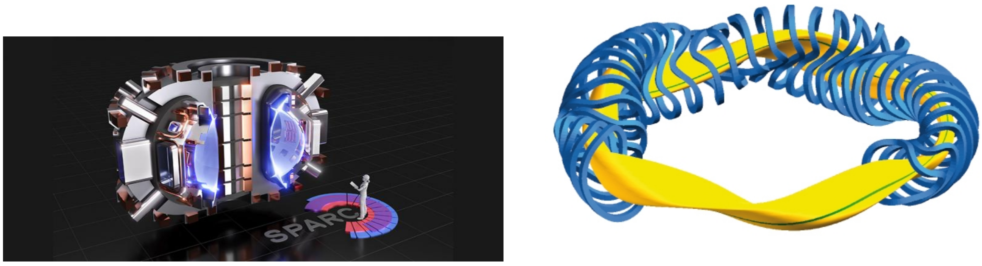

Figure 1.5: Sketch of SPARC [12] and W-7X [13]

The different approach proposed by these solutions seems to make the reality of using fusion reaction to produce electric energy much closer than in the EU-DEMO scenario. Of course, none of them have reached practical objectives yet, but also the fact that lots of private companies invest plenty of money in them is promising.

Chapter 2

Motivations of the work

2.1 The power exhaust problem in Tokamaks

After having described the main challenges that must be faced to reach the goal of producing electric energy from the fusion reaction, a focus will be performed on the specific issue that this thesis is going to analyze: the power exhaust.
First of all, it is fundamental to describe the power balance of the system considering all the contributions in terms of heat and particle flux, that have to be removed from the surface in contact with the plasma.

The power produced by the fusion reactions is carried by alpha particles (Helium nuclei) and neutrons which are the direct products of the fusion reactions, to which the energy furnished by auxiliary heating systems, has to be added. While the energy transported by neutrons does not contribute to the plasma energy balance, the external and alpha particle ones have to be balanced by a sink that is represented by the traditional heat transfer mechanisms of radiation, conduction, and advection. Radiation is an isotropic mechanism and consequently will be directed uniformly in every direction, whereas the other two are anisotropic and strongly influenced by the magnetic field. Actually, these mechanisms are based on the motion of the charged particles of the plasma, which follow the magnetic field lines. As stated in paragraph 1.2, the system of magnets generates a complex structure of the magnetic field, as depicted in figure 2.1, where a series of nested magnetic surfaces are produced. In the same picture is also represented the system of three coordinates that will be used in the following chapters: the toroidal, indicated by ρ, the poloidal by Θ, and the radial by Ψ.

Moreover, two separate regions can be identified in the poloidal section: an internal - core - region and the Scrape Off Layer (SOL), surrounding the first one. This configuration, called *divertor configuration*, represented in figure 2.2, has the

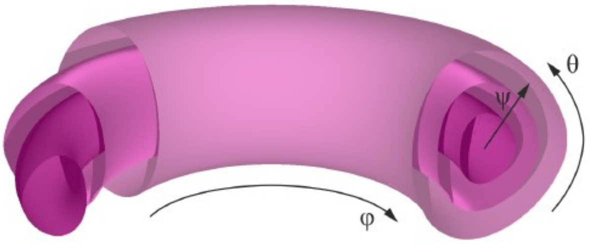

Figure 2.1: Representation of nested magnetic surfaces developing in a Tokamak configuration [15].

main advantage of deflecting the huge flux of particles and heat only on the lower part of the tokamak, the so-called *divertor*.

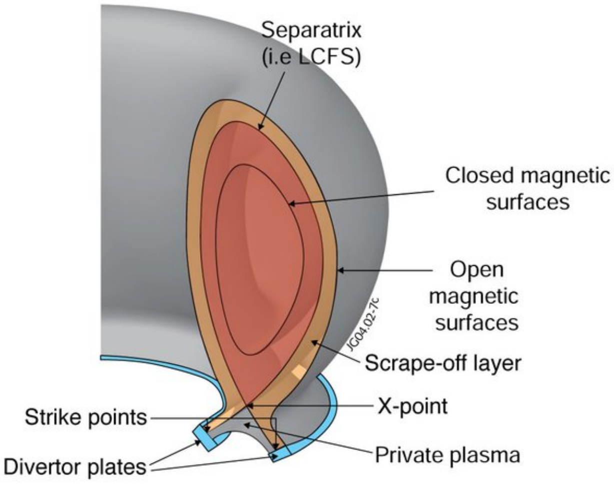

Figure 2.2: Sketch of the two regions of the plasma, namely the core and the SOL, divided by the Separatrix. Also, the location of the divertor is reported at the bottom of the figure. [16]

This occurs thanks to the nature of the magnetic field lines, which come out to be closed in the core region, and open in the SOL. This structure gives rise to very different transport mechanisms in the two areas, being mainly slow and diffusive in the central part and instead fast in the SOL region. In this external area, in fact, particles are led by the strong gradient arising in the open magnetic field lines and move much more quickly along them, with a motion that gets a two-dimensional nature, mostly along magnetic lines but also across them. Hence, the complete trajectory of particles starts in the core region where they are generated by fusion reactions thanks to the higher density and temperature, reaches the *separatrix*, and then follow the open field lines until colliding with the *strike-points* on the bottom part of the machine. Here, the engineered surfaces of the *divertor* have the job of handling the high flux coming from the SOL and exhausting it.

2.2 Atomic processes at the plasma edge and role of the divertor

The physics that occurs in the region very near to the plates of the divertor, called *plasma edge*, is very complex but fundamental to realize the mechanisms that permit the removal of the power.

The nature of the magnetic field causes the generation of a thin layer of relatively cold plasma (several tens of eV, compared to several tens of keV expected in the core) that touches the wall of the divertor all along the toroidal direction. When this narrow flux of particles arrives in the proximity of the plates, different atomic processes between charged particles of the plasma and neutrals from the wall arise, being mainly beneficial to the exhausting of the power but also potentially harmful.

Depending on the energy of charged particles hitting the wall and on the mass of the ones that compose the wall itself, some neutral atoms can be sputtered and extracted from the plates, entering the edge plasma. Here, different mechanisms can occur: they can exchange momentum and energy with charged particles, making the plasma lose power, or they can get ionized. That is: due to the high temperature, electrons of the neutral particles can be extracted, generating ions and also releasing energy through radiation processes like Bremsstrahlung and line radiation, further decreasing the energy of the plasma and reducing the temperature at the wall. Finally, electrons and ions can recombine and generate a neutral particle, which again could undergo one of the above mechanisms (a process which becomes increasingly probable at low temperatures). It is important to remember that, if the neutrals or the ionized particles from the SOL reach the core plasma, they reduce the power also in this region by the same mechanisms enhanced by rising temperatures. If this occurs the plasma is *polluted* and it could not have enough energy to make the fusion reaction occur, potentially leading to the shut down of the plasma.

In this framework, the main aim is to maximize the effects that these phenomena could give at the edge to decrease the power flux sustained by the divertor, and, at the same time, to maintain them confined in the very edge region, not polluting the core plasma. This can be done by studying accurately the composition of the divertor plasma-facing component so that the neutrals that will be extracted could decrease the temperature at the edge but will not reach the core plasma in a too big concentration. The most promising solution to this problem is the usage of Tungsten as plasma facing component for the divertor plates of ITER, but in the past also Beryllium, for example, has been adopted.

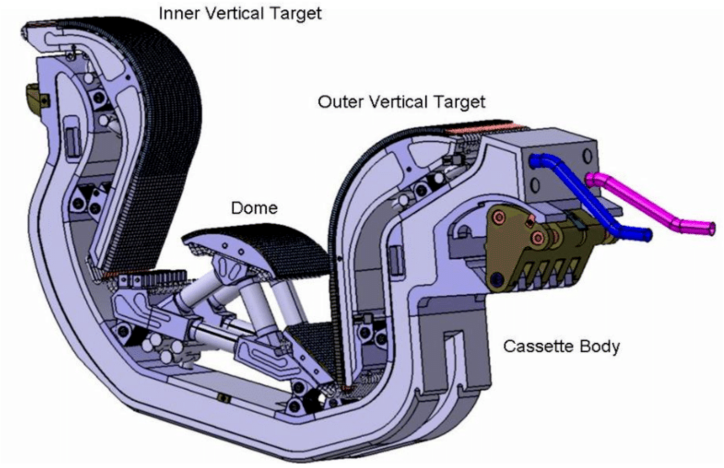

Figure 2.3: Representation of the structure of a cassette of the divertor, with the three different components of the inner and outer vertical target and the dome. [17]

To understand the order of magnitude of the power that has to be exhausted at the divertor plates, some estimation for the ITER case [18] depicts that around 60% of the total heating power (150 MW) will flow inside the SOL region and 2/3 of this will be directed through the outboard divertor, which will finally have to exhaust around 30 MW/m^2 (the ITER divertor's wetted area is planned to be around 2 m^2). Extrapolating these percentages for the EU-DEMO scenario [19], which is going to produce 500 MW of total heating power, it becomes clear that some very effective and enhanced method for exhausting the power at the divertor has to be adopted for this enormous machine, and one of them is the implementation of Liquid Metal Divertors (LMDs).

2.3 Liquid Metal Divertors

When dealing with the huge amount of power produced in the EU-DEMO scenario, it becomes fundamental finding alternative solutions to address the problem. The concept of Liquid Metal Divertors (LMDs) consists of employing a Capillary Porous Structure (CPS) [20] as plasma-facing component inside which a liquid metal is flowing and able to evaporate, continuously replenished passively by a recirculation loop driven by capillary forces.
The biggest advantages of using Liquid Metal Divertors are that it is possible to

avoid thermo-mechanical failure of the plasma-facing structure, that in the case of solid divertor is subjected to erosion, macrocraking, melting, and embrittlement, and the gaining of two extra cooling mechanisms. In fact, the liquid metal, due to the heat load coming from the plasma evaporates, and the neutral particles collide with ions and electrons of plasma, decreasing its temperature. At this point, a recondensation of the liquid metal particles occurs and they come back to the porous structure, where are collected and led to flow into the reservoir. The latter is located at the bottom of every single cassette composing the divertor, to ensure continuous replenishment of the liquid metal and heating it in order to maintain the liquid state.

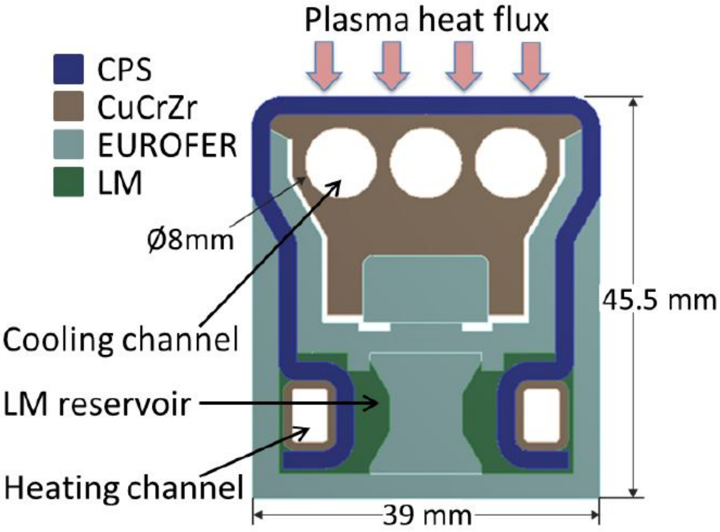

Figure 2.4: Structure of the ENEA concept of the Liquid Metal Divertor cassette [20]

The evaporation/condensation phenomena represent the two extra cooling mechanisms, also called *evaporative cooling* and *vapor shielding*, because a sort of cloud of particles is basically produced in front of the divertor's plates (fig. 2.5). This effect is the base of the so-called *self-healing* capability of LMD since it can protect the surface of the divertor itself, theoretically leading to zero net erosion. Moreover, the structure of each cassette permits, as said, to have a continuous passive replenishment of liquid metal thanks to the capillary forces, which are also able to counteract the **J**x**B** forces which would lead metallic components (like liquid metals) going through the core plasma, attracted by the magnetic field lines.
What has to be avoided in fact, is the occurrence of the liquid metals' particles (in the form of droplets or vapor) to enter inside the core plasma and pollute it. The atoms that are not re-condensing could enter the SOL region and eventually

the core, where they can determine significant core plasma radiation, possibly enough to shut it down (as better described in the previous paragraph 2.2). This effect is typically called *plasma contamination* and is mainly related to high-Z impurities, which may even remain not fully ionized in the core plasma and so dissipate energy via line radiation on top of Bremsstrahlung. The other effect that has to be prevented is the *plasma dilution*, which consists in the decrease of the main plasma ions due to the accumulation of impurities' ion, in order to ensure the *quasi-neutrality* condition ($n_e = n_i$). This phenomenon is mainly related to low-Z impurities, like He ashes for example, and is of course dependent on the density concentration of the impurity. A more accurate description of impurities' effects on the core plasma is addressed in the specific section 3.4.

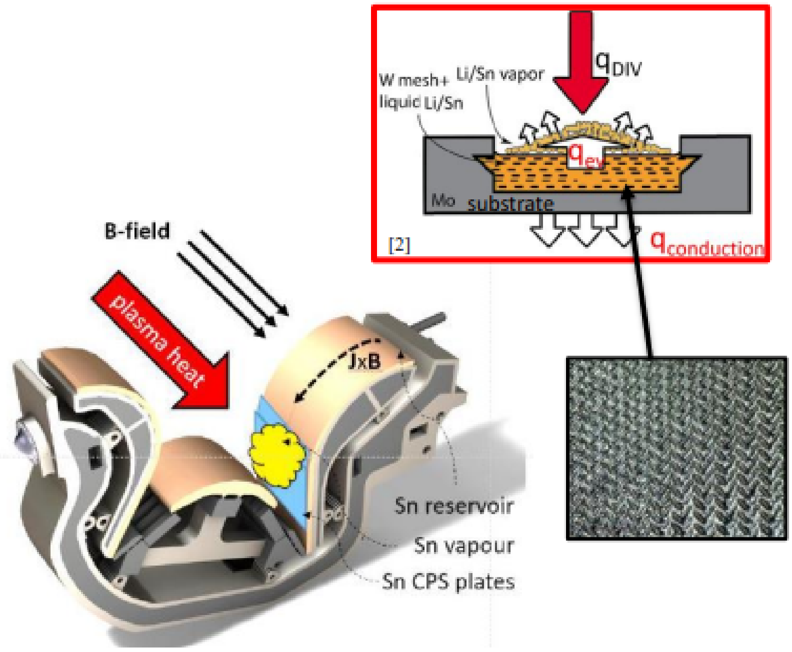

Figure 2.5: Sketch of the Liquid Metal Divertor Capillary Porous Structure and of the extra-cooling mechanisms occurring at the surface. [21]

Trying to balance these two effects of dilution/pollution while employing a Liquid Metal Divertor configuration is the most difficult part of the challenge, and the liquid metals that have been considered for this purpose are Lithium and Tin. On one hand, Lithium is a low-Z impurity, with a maximum charge of 3, so it is very easily ionized while entering the plasma, but it could also generate dilution, accumulating in the core and reducing the fusion yield. Moreover, it has a high vapor pressure, producing excessive evaporation at a too-low temperature (600 $°C$). On the other hand, Tin has a very high maximum charge (50) and a lower evaporation rate. This means that even if it evaporates less than Lithium, a single atom can radiate and be ionized many times, being more efficient in decreasing the temperature. Of course, more easily it could reach the core plasma not fully ionized and pollute it.

A deep focus on the different effects on the core plasma of these two liquid metals is the main scope of this thesis work, and it will be developed in the next chapters.

Chapter 3

Transport in Tokamaks

The previous chapters have been devoted to describe the general framework of this thesis, giving basic information about the comprehensive engineering and physical aspects. In the following paragraphs, transport phenomena that regulate the motion of particles inside the Tokamak will be analyzed, with the main aim of understanding the reasoning behind the usage of different codes (4) and the setup of the simulations (5).

Briefly introducing the main useful notions, a fusion plasma is made by ionized particles in thermal equilibrium, whose trajectory is regulated by the combination of magnetic fields produced by the complex structure of magnets previously explained in chapter 1 and drifts arising due to electric and magnetic field fluctuations as well as the toroidal geometry. The main property of a plasma is that, apart from a very small distance near each particle (the *Debye length*), any electric field is shielded, and this gives rise to the condition of *quasi-neutrality.* Considering this phenomenon, it becomes more interesting to study the *collective* effects that dominate the plasma, regardless of what happens on the very small scale around a single particle. These phenomena are driven by long-range effects of electric and magnetic fields inside the plasma, that, with these assumptions, can be seen as a fluid in which also magnetic forces are present.

The MagnetoHydroDynamic (MHD) model describes the equilibrium condition of a magnetized plasma considering it as a single fluid. The model implies the definition of a system of equations representing the conservation of particles, momentum, and energy in the system, driven by magnetic and hydrodynamic forces.

Having stated these main concepts, for the purposes of this work, it will be interesting to depict diffusive phenomena that regulate the transport of particles, momentum, and heat once the equilibrium configuration is reached. In the following chapters, these mechanisms will be described, starting from the simplified case of classic transport in a 1D cylindrical magnetized plasma (3.1), going into the description of effects arising in the toroidal configuration (3.2) and finally quoting the main anomalous phenomena (3.3).

3.1 Classical Transport

The main aim of this part is to describe the transport of mass, energy, and magnetic flux in a cylindrical plasma through a set of *diffusion-like* equations for each quantity.

The cylindrical coordinate system that is used is schematically represented in figure 3.1, where Z is the direction of the magnetic field B, r the radial direction of the plasma, and Θ the poloidal direction.

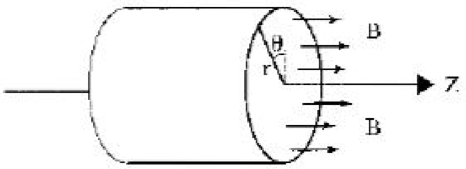

Figure 3.1: Coordinate system of the cylindrical plasma [22].

Under these conditions, the MHD equations that define the balance of forces in the cylindrical plasma can be written as 3.1, according to [1], where n, T, p, v are respectively the density, temperature, pressure, and velocity of the plasma, B is the magnetic field, μ_0 the magnetic permeability in the vacuum, q the heat flux and S a generic source term of energy.

$$\begin{aligned} \frac{\partial n}{\partial t} + \frac{1}{r}\frac{\partial}{\partial r}\left(rnv\right) = 0 \\ \frac{\partial}{\partial r}\left(p + \frac{B_z^2}{2\mu_o}\right) + \frac{B_\theta}{\mu_o r}\frac{\partial}{\partial r}(rB_\theta) = 0 \\ 3n\left(\frac{\partial T}{\partial t} + v\frac{\partial T}{\partial r}\right) + \frac{2nT}{r}\frac{\partial}{\partial r}(rv) = -\nabla\cdot\mathbf{q} + S \end{aligned} \tag{3.1}$$

These equations represent the conservation of mass, momentum, and energy and they can be rewritten in a simpler form under the following assumptions. Introducing Ohm's law for a magnetized plasma:

$$E + v \times B = \eta_\perp J_\perp + \eta_\parallel \frac{J_\parallel}{B}\mathbf{B} \tag{3.2}$$

$\eta_\parallel$ and $\eta_\perp$ are the electric resistivity component of the plasma ($\eta \propto T_e^{-3/2}$) respectively in the same direction of the magnetic field and in the perpendicular

one, similarly to the plasma current $J_{\parallel}$ and $J_{\perp}$.
Assuming that the magnetic field in the axial direction Z is the dominant component and almost constant, integrating the B_z component over the radial direction and considering $J_{\parallel} \sim J_{\perp}$ [1], the set of equations becomes:

$$\begin{aligned} \frac{\partial n}{\partial t} &= \frac{1}{r}\frac{\partial}{\partial r}[rD_n(\frac{\partial n}{\partial r}+\frac{n}{T}\frac{\partial T}{\partial r} + \frac{n\eta_{\parallel}}{\beta_p\eta_{\perp}}\frac{n}{rB_\theta}\frac{\partial rB_\theta}{\partial r})] \\ 3n\frac{\partial T}{\partial t} &= \frac{1}{r}\frac{\partial}{\partial r}(rn\chi\frac{\partial T}{\partial r}) + S \\ \frac{\partial rB_\theta}{\partial t} &= r\frac{\partial}{\partial r}(\frac{D_B}{r}\frac{\partial rB_\theta}{\partial r}) \end{aligned} \tag{3.3}$$

where D_n and D_B are the diffusion coefficients, related respectively to the particle diffusion and to the magnetic field one. Finally, χ is the thermal diffusion coefficient, related to the diffusion of heat. The definition of these two coefficients, according to [1], are reported in 3.4 where B_0 is the constant magnitude of the magnetic field along the Z direction:

$$\begin{aligned} D_n &= \frac{2nT\eta_{\perp}}{B_0^2} \\ D_B &= \frac{\eta_{\parallel}}{\mu_0} \end{aligned} \tag{3.4}$$

The three equations in 3.3 represent the set of coupled non-linear partial differential equations which describes the classical transport in a 1D cylindrical plasma. The main difficulty is to calculate the diffusive coefficients, which generally depend on the transported quantities but can be approximated by studying the collisional phenomena that generate the diffusion. In fact, the motion of particles perpendicular to the magnetic field is driven by Coloumb collisions and the strategy used to evaluate the diffusion coefficients consists of approximating the mean-free path between collisions considering the ratio between a characteristic length $r_{L,e/i}$ to the power of two over the characteristic time $\tau_{i,e}$ as reported in 3.5.

$$\begin{aligned} D_e &= \frac{r_{Le}^2}{\tau_e} \\ D_i &= \frac{r_{Li}^2}{\tau_i} \end{aligned} \tag{3.5}$$

r_L is the *Larmor radius*, the radius of the spiral trajectory of particles around a magnetic field line, and according to Lorentz's force, this is bigger for ions than for electrons. Hence the ions' diffusion will be faster than the electrons' one.

Similarly, χ_i and χ_e, which represent the heat diffusion rate, are very different between ions and electrons again due to the bigger gyroradius of ions.

$$\begin{aligned}\chi_i &= \frac{r_{Li}^2}{\tau_{ii}} \\ \chi_e &= \frac{r_{Le}^2}{\tau_{ee}}\end{aligned} \tag{3.6}$$

Solving the set of the coupled transport equations 3.3 means obtaining profiles of density, temperature, and poloidal flux but before doing that is important to consider the other phenomena occurring in the plasma once the more realistic toroidal geometry is considered.

3.2 Neoclassical transport

A more complete description of the transport in a tokamak involves the consideration of being in toroidal geometry. This design in fact generates the so-called *neoclassical* effects, which increase by nearly two orders of magnitude the rate of transport of particles. As it has been stated in the previous chapter, the diffusion coefficients depend on the step size between two collisions. In the cylindrical configurations, particles are constrained around their gyro-radius, while in the toroidal geometries drifts arise and increase the radial excursion. Moreover, in the toroidal configuration, the effect of the mirror force gives rise to a fundamental phenomenon of *trapped particles*, which will be better described in the following paragraphs.

In particular, different *collisionality regimes* of transport could arise, depending on the collision frequency: the aim of neoclassical transport is to solve the drift kinetic equation, which describes analytically the motion of single particles, in these regimes. In the following, the parameter that discriminates the existence of a specific collisional regime will be described, going then to analyze the three main resulting regimes, namely the *banana*, the *plateu*, and the *Pfirsch-Schluter*.

The parameter that characterizes the different regimes is the *transit frequency* ω_t defined as:

$$\omega_t = \frac{v_T}{qR} \tag{3.7}$$

where v_T is the thermal velocity of particles, and qR is instead the parallel distance around a flux surface (being q the safety factor and R the major radius).

In particular, this value, characteristic of the plasma condition, has to be compared to the Coulomb collision frequency ν. In fact, writing the ratio:

$$\frac{\nu}{v_T/qR} \tag{3.8}$$

it is possible to recognize that $v_T/\nu = \lambda$ and $qR \sim L$, so that the previous formulation (3.8) can be written as:

$$\omega_t = \frac{L}{\lambda} \tag{3.9}$$

This ratio can be finally used to understand in which collisional regime the plasma finds itself. If it is much bigger than one, it means that the Coloumb collisions are so frequent to prevent particles to complete their orbits while moving in the toroidal direction, leading to the so-called *Pfirsch-Schluter* regime. In the opposite case, the collisionality in the plasma is lower, and particles are able to complete their orbits, giving rise to two possible regimes, the *Banana* or the *Plateau* ones, depending on the *inverse aspect ratio* $\epsilon = \frac{R_0}{a}$.
For the sake of clarity, the above mentioned conditions are here reported:

$$\begin{aligned} \frac{L}{\lambda} = \frac{\nu}{v_T/qR} >> 1 \quad Pfirsch - Schluter\ regime \\ \frac{L}{\lambda} = \frac{\nu}{v_T/qR} << 1 \quad Banana\ or\ Plateu\ regime \end{aligned} \tag{3.10}$$

A focus on the three different regimes is now developed, describing the main effects arising in the trajectory of particles.

3.2.1 Banana regime

The condition of the banana regime is the regime aspired for operating conditions of plasma, since in this situation, the majority of particles are trapped in their orbits thanks to the mirror force and consequently well confined.
The boundary to differentiate this regime from the Plateau is defined by the aspect ratio ϵ:

$$\frac{\nu}{v_T/qR} << \epsilon^{3/2} \tag{3.11}$$

Given the defined collisionality limits, the main reason why this effect happens is that, due to the radially decreasing toroidal magnetic field, the parallel velocity of particles in the outer region of the plasma is smaller and the condition for being trapped by the magnetic mirror effect (see [1]) is satisfied.

It can be demonstrated that the step size between two collisions in the *trapped* condition is higher by a factor $1/\epsilon$ with respect to passing particles (completing a "circular" trajectory without their trajectory being reversed).

In this regime the mirror effect is not limited by any too frequent collisions and particles are able to reverse their trajectory and enclose them without being interrupted. In the toroidal configuration, this effect results in a banana orbit, better represented in figure 3.2.

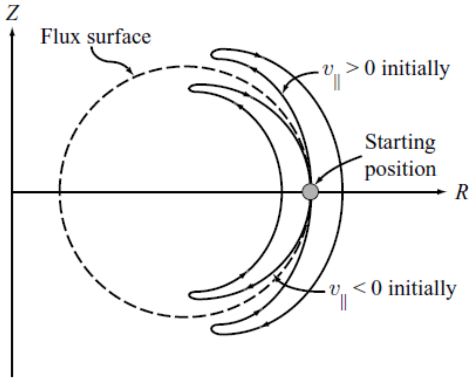

Figure 3.2: Banana orbits for a particle with $v_{\|} > 0$ or $v_{\|} > 0$, leading to a correspondent outward or inward shift [1].

A fundamental effect that arises in this regime is the generation of the *bootstrap current*, due to friction between passing and trapped particles. In fact, passing particles are able to carry an amount of current theoretically of the same amount of the plasma current and in the same direction. This would lead to the potential capability of confining efficiently the plasma without the need for external current drive power. This is another reason why the banana regime is the one that is expected to be used in fusion reactors, decreasing the amount of external power in the power balance.

3.2.2 Plateau regime

The condition to be in the *plateau regime* is satisfied for the case of low collisionality and in particular if the characteristic ratio is within these limits:

$$\epsilon^{3/2} << \frac{\nu}{v_T/qR} << 1 \tag{3.12}$$

The main difference with the banana regime is that in this case the collision frequency ν is slightly higher leading to the incapability of trapping particles that instead are all *passing*. These particles dominate the radial transport which turns out to be independent of the collision frequency. This is the reason why is called *plateau* regime because when considering the diffusion coefficient in different regimes in dependence on the collision frequency, the following behavior can be seen:

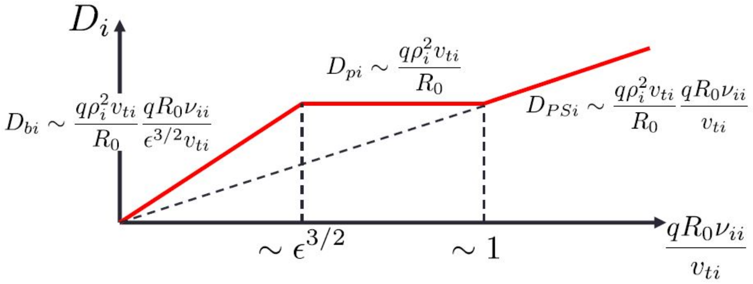

Figure 3.3: Diffusion coefficient in terms of collisionality. [23]

where the first linear phase represents the banana regime, in which the diffusion of particles increases with collisional rate, then there is the phase of plateau regime in which diffusion coefficient remains constant, and finally, the Pfirsch-Schluter in which collisionality increases.

3.2.3 Pfirsch-Schluter regime

In this regime the collisionality is very high, such that the diffusion coefficient can be evaluated solving the Braginskii's equation and not the kinetic one as in the other case. What physically happens in this situation, that usually occurs in the edge plasma, is that particles collide that much not to being able to enclose a single orbit because collision frequency ν exceed the transit one ω_t.
A better raffiguration of this behavior is represented in figure 3.4, where the random walk of particles is always interrupted, leading to an increase of the diffusion coefficient of the order of q^2 with respect to the classical theory [22].

3.3 Turbulent transport

Experimental evidence has proven that neither classical nor neoclassical transport is enough to describe completely what happens in the toroidal geometry of a magnetized plasma. Some anomalous effects must exist, and they should be responsible for the extra mechanisms of transport of particles, energy, and momentum. These effects are due to temperature or density gradients, but also to micro MHD instabilities on magnetic or electric fields and have the average effect of increasing the radial transport of particles.
When these temperature or density gradients are strong enough, turbulent effects

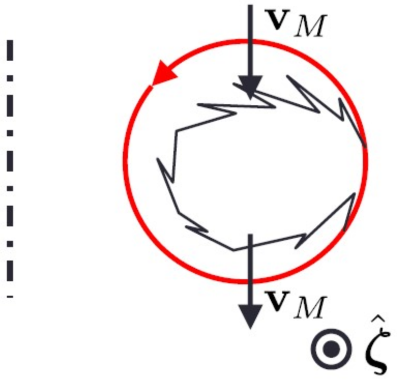

Figure 3.4: Pfirsch-Schluter orbit [23].

prevail on single particle motion, generating a source of thermodynamic energy, resulting in convective vortexes.

The way in which these turbulences arise in the plasma is through *drift wave instabilities*. Due to the pressure gradient across the magnetic field direction, naturally occurring in magnetically confined plasmas, both parallel and perpendicular instabilities appear, originating three-dimensional effects of turbulence. In this chapter, the most common instabilities driven by drift waves will be analyzed, namely the *ion temperature gradient mode (ITG)*, the *electron temperature gradient mode (ETG)*, and the *trapped electron mode (TEM)*.

3.3.1 ITG and ETG mechanism

These types of turbulence are respectively driven by the gradient of ion or electron temperature. The mechanism consists of a temperature perturbation that, in turn, generates a perturbation also in the density. Passing electrons try to neutralize the perturbation to restore the initial condition leading to the formation of an electrostatic potential. The disturbance on the electric field induces, among other effects, an $E \times B$ flow, which mixes the hot and cold regions of plasma, enhancing even more the initial perturbation.
The toroidal ITG mode is the most effective turbulence mechanism, leading very efficiently heat and particles toward the edge region, from the High Field Side (HFS) of the poloidal section to the Low Field Side (LFS) (3.5). This phenomena influence mainly ion transport but is able also to enhance the electron transport channel, especially at high density.

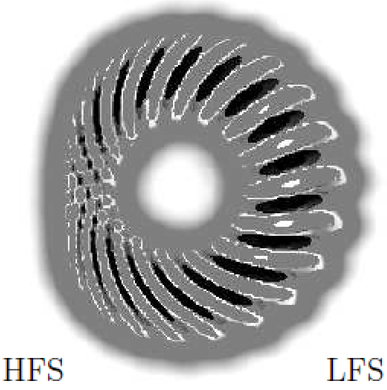

Figure 3.5: Sketch of the electrostatic perturbations in ITG modes in a poloidal section of plasma [15].

3.3.2 Trapped electron mode (TEM)

The TEM mechanism is generated both by electron temperature and density gradients and generates a similar mixing effect to the ITG and ETG modes but in the opposite direction. This could lead to the generation of inward particle flux and a consequent peaking of the density in the core. As for the previous case, figure 3.6 represents the poloidal section of plasma in the case of TEM mode.

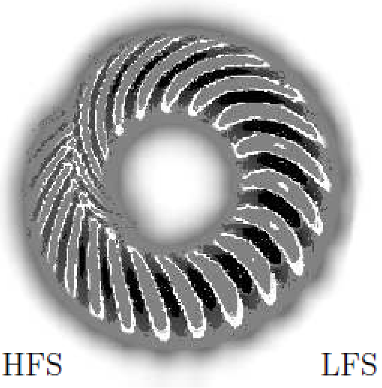

Figure 3.6: Sketch of the electrostatic perturbations in TEM modes in a poloidal section of plasma [15].

However, TEM modes are strongly dependent on the fraction of deeply trapped particles, so on the plasma regimes.

3.4 Impurities behavior

Impurities in a plasma are defined as all those species which are not fuel for the fusion reaction, and that can lead to the decrease of fusion power due to dilution and radiations.
Their transport is driven by the same collisional events explained in the previous chapters, but their higher charge and mass with respect to deuterium and tritium ions lead to the generation of some different mechanisms. Nevertheless, their radial transport will be driven by temperature and density gradients of the main plasma and in particular this effect is described by:

$$\frac{1}{n_Z}\frac{dn_z}{dr} = \frac{Z}{n_i}\frac{dn_i}{dr} + \frac{\alpha}{T}\frac{dT}{dr} \tag{3.13}$$

where the subscript Z stays for the impurity species, and α is a parameter accounting for thermal forces.

The main difference between the background plasma and impurities transport lies in the fact that collisions within ions and impurities are more frequent than the ones between ions and electrons, and in particular, this frequency, which is seen as a *friction*, scales as $\propto n_Z\ Z^2$. This means that, with the increase of the charge and accumulation of the impurity, collisions increase that much to make the Pfirsch-Schluter regime the dominant one. This, in turn, leads to the possibility of treating impurity transport with the fluid approximation, but separating their study from the transport of the main plasma.

As for the main plasma species, also impurities are affected by neoclassical transport, which anyway is not completely sufficient to describe their motion. Anomalous effects like ITG and TEM arise, but unfortunately, an analytical formulation for turbulent impurity transport is still not found. Surprisingly, a very simple empirical formula like 3.14 can be used to model the major behavior of impurities particles and to describe their radial flux Γ_Z.

$$\Gamma_Z = -D\nabla n_z + n_z V \tag{3.14}$$

D_z is the *diffusion coefficient* related to the impurity density gradient, and V is the *convective coefficient*, also called the *pinch velocity.* These two coefficients depend on the background plasma parameters, which, however, are affected by the impurity's density accumulation, driven by the transport coefficients, giving rise to a feedback effect.
The very general outcome of the motion of impurities is that, in order to fulfill the ambipolarity condition (for which electrons and ion fluxes diffuse at the same rate), they have to move in the opposite direction with respect to the main plasma

species. This effect can be better explained also by analyzing the typical radial gradients of temperature and density of tokamaks, which are usually negative. In fact, following the equation 3.14 and considering that the convective coefficient V is usually larger than the diffusive coefficient, directly proportional to the charge of the impurity ($V = ZD$), this implies a positive diffusive coefficient - outward directed - and a negative convective flux - inward directed. Consequently, the inward pinch of impurity becomes more and more relevant as the charge increases [24].

However, as previously stated, also turbulent effects have to be considered. The most important instabilities arising in plasmas are the ITG and TEM modes. These mechanisms are strongly dependent on the ion and electron logarithmic gradients of temperature and density ($L_{Te,i}$ and $L_{ne,i}$), and it has been seen [25] that in the case of very high R/L_{Te}, both the diffusive and convective coefficients are positive, pushing to the edge impurities. This condition can be reached for example in the case of high electron heating for example, when ECRH (Electron Cyclotron Resonance Heating) is employed and represents a particular case in which impurities could potentially not accumulate in the core plasma.

The most important quantities that are analyzed for the purposes of this thesis are the impurity density accumulation and the radiated power of each species. In fact, as stated in chapter 2, the main motivation of this work is to assess if the power radiated by the impurity due to line, recombination, and Bremsstrahlung radiations is enough to affect negatively the power balance and shut down the plasma.
The formulation for the radiated power of a specific impurity is described by

$$P_{rad} = n_e n_{imp} \sum_k f_k (L_k^{line} + L_k^{rec} + L_k^{Brm}) \tag{3.15}$$

where the summation term represents the total *radiative cooling rate* L_Z over the k ionization stages, and f_k is the fraction of each impurity ionization state defined as n_k/n_{imp} [26]. The radiative cooling rate L_Z quantifies the losses of the system due to the atomic processes and it is a function of electron temperature and of *dwell time* τ. By definition, the dwell time is the characteristic time spent by a particle in an isothermal region of plasma, hence it is related to the velocity with which each particle is transported inside the plasma. When the dwell time tends conceptually to infinity, the species is called to be in *coronal-equilibrium*. In this state, the transport effects are neglected, and depending only on the temperature of the plasma, the impurity will have different values of radiative losses (defined by L_Z) and *average charge* $< Z >$. It is defined as:

$$< Z > = \sum_k k \cdot f_k \tag{3.16}$$

representing a weighted charge of the species, considering the abundance of each ionization stage, being k the correspondent charge. This parameter is also a function of electron temperature as shown in figure 3.7. Here, the fractions of Tin (f_k) at different ionization stages are reported for increasing temperatures.

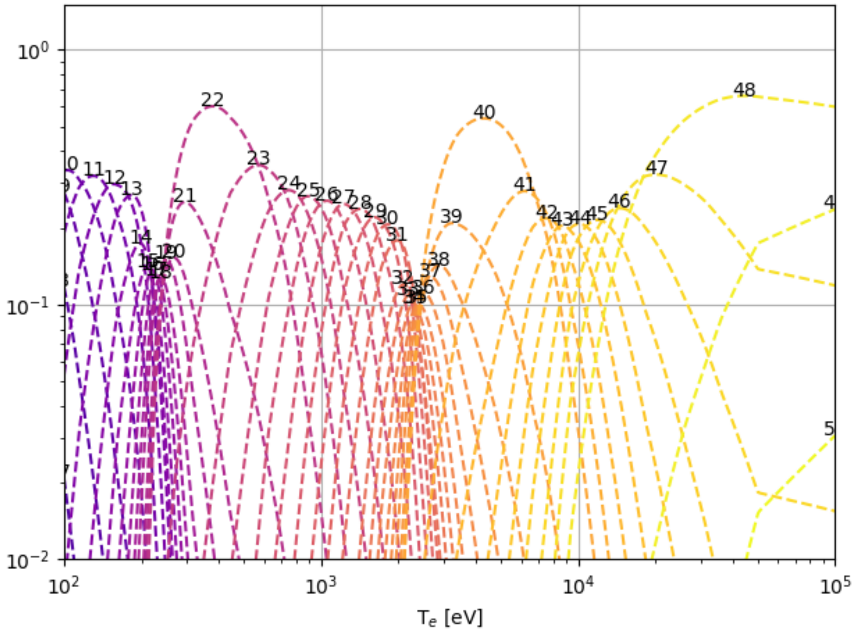

Figure 3.7: Fraction abundance of each ionization stage of Tin at different temperatures. The small numbers labeling each line of the graph represent the charge state of the impurity.

If one looks at the same parameter for Lithium, the graph would be always around 3, since Lithium is fully ionized at very low temperatures.

In figure 3.8, total radiative cooling rate functions are reported for different impurities.

As is shown in figure 3.8, with the increase of the atomic number, the impurities radiate more. This is due to the fact that the species have more electrons to be stripped and excited.
It is fundamental to consider the difference between the type of prevalent radiations, in light or heavy impurities. In fact, the Bremsstrahlung radiation is due to the interaction between an electron and an impurity ion, which leads to the loss of energy by the electron that emits it in terms of a continuum radiation. The power loss by Bremsstrahlung is more relevant at high temperatures and has the following

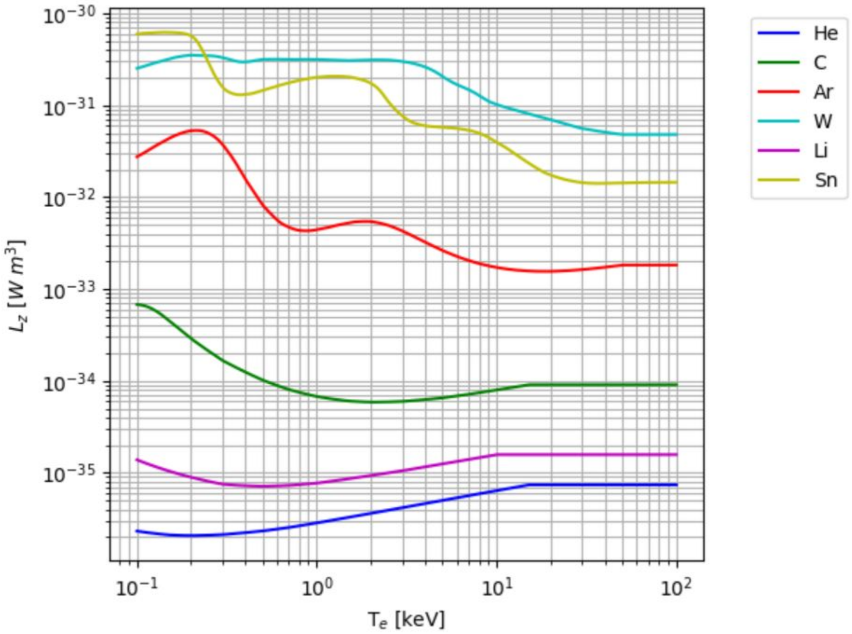

Figure 3.8: Radiative cooling rate L_Z functions depending on the impurity species and on temperature. This graph has been done post-processing the atomic data extracted by the *Aurora* code by F.Sciortino [27]

formula according to [1]:

$$S_B = C_B Z_{eff} n_e^2 T_e^{1/2}\ [W/m^3] \tag{3.17}$$

where C_B is a constant value and Z_{eff} the effective charge, defined as:

$$Z_{eff} = \frac{\sum_j Z_j^2 n_j}{n_e} \tag{3.18}$$

It is possible to recognize the dependence on the charge of the impurity and the correspondent abundance and understand that, for heavy impurities, Bremsstrahlung radiations will be more relevant than for light ones, due to the higher deflection that induces in the colliding electron.
Line radiation instead, is associated with the excitation and de-excitation of the electrons which release energy, hence, when a species is fully ionized is no more possible to line-radiate and the only radiation occurring will be the Bremsstrahlung. Considering the nature of these types of radiations it is possible to assess that the total radiation emitted will be bigger for heavier impurities and that for them the contribution of line radiation will be prevalent with respect to the Bremsstrahlung one since more electrons are available to be stripped by atoms. Instead, for lighter

impurities the majority of radiated power will be done in terms of Bremsstrahlung.

It is possible to recognize this behavior by looking at the following figures 3.9 and **??**, where the total radiated power of Lithium and Tin are compared, splitting the contribution of line radiation and continuum, which takes into account radiations due to Bremsstrahlung and recombination.

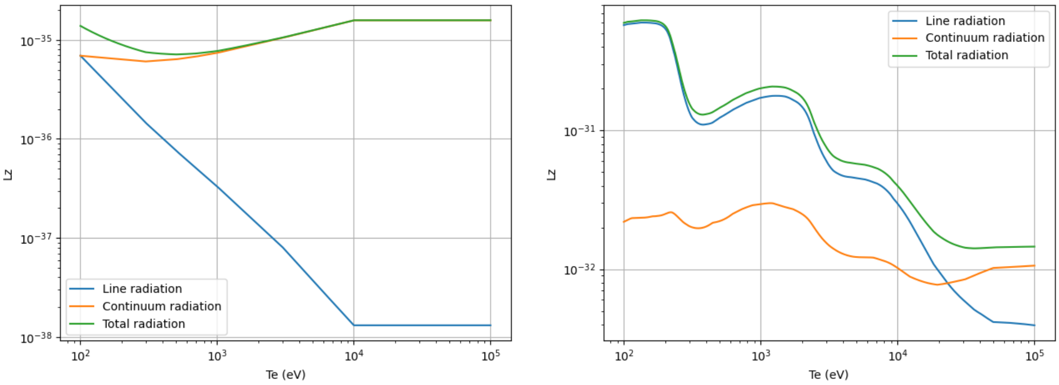

Figure 3.9: Total, line, and continuum radiation of Lithium in the right-hand graph and of Tin in the left-hand, as a function of the temperature and at coronal equilibrium.

It will be seen in chapter 5.1 how to define and use these values of radiative cooling functions and average charge to calculate the radiated power of each impurity.

Chapter 4

Core transport modelling

The aim of this section is to describe the main tools used to simulate the transport of particles inside the core plasma. The modeling of the physical effects studied with theoretical and analytical models is a crucial step for the advancement of research and has its roots in the development of numerical codes. The main goal, for the current application in plasma physics, is to realize an instrument that can be used to predict the behavior of plasma in different conditions so that technical and engineering choices can be made conscientiously.
Translating the concept into the specific framework of this thesis, a model that predicts accurately the motion of impurity particles all the way from the target to the core is needed, so that correct previsions on the problem of impurities accumulations and possible shutdown of the plasma for the EU-DEMO project are made.

This is indeed the strong motivation and boldness of this work: not only modeling the transport of impurities in a huge reactor such as EU-DEMO but also trying to reach an integrated characterization of their path, starting from the behavior in the SOL region once emitted by the divertor, and consequently reaching the core. A specific description of the codes used to model the transport phenomena in the core plasma will be done in the following chapters, including STRHAL, even if it was not used in the end, but which has crucial strengths, worth to be quoted. Also, a brief analysis of the strategy and motivations employed to reach an integrated characterization of the path of impurities from the target to the core is presented.

4.1 The ASTRA code

The ASTRA (Automated System for TRansport Analysis) code is a flexible system capable of setting predictive or interpretive transport problems in the confined plasma [28]. It is a programmable code with a modular structure which makes it very attractive to solve a wide variety of transport problems, having the possibility of tailoring and adding modules for the inclusion of specific physical phenomena.

The 3D transport problem is reduced to a 1.5D one, taking advantage of the axisymmetry of the Tokamak. In fact, as described in chapter 2, the focus will be on radial transport, as the most relevant for confinement purposes. The close nature of these lines in the core plasma maintains particles on the same *magnetic surfaces* at the same pressure, making the gradients in the toroidal direction almost negligible with respect to the radial ones. For this reason, the domain considered in the core transport codes is one-dimensional but the magnetic surfaces, being traced by the magnetic field, evolve in time, and this must be taken into account in the simulation. To reach this objective the ASTRA code is equipped with an equilibrium solver capable of evaluating the equilibrium configuration solving the Grad-Shafranov equation **??** and calculating the nested magnetic surfaces (2.1) shape. This produces the metric coefficients in the solved equations and gives the name of "1.5 D" (rather than 1 D) to this kind of codes. Once done this, properties are volume-integrated over each surface giving as output a single radial value across the normalized radius of the plasma ρ.

Having done this foreword, it is possible to describe the system of equations that ASTRA solves (4.1), as described in [28]: 1D diffusion equations respectively for electron density n_e, ions and electron temperature T_e, T_i, and poloidal flux ψ (related to the plasma current). It does it assuming that the plasma is in equilibrium conditions, neglecting relaxation processes, which occur way faster than transport ones.

$$\begin{cases} \frac{1}{V'}\left(\frac{\partial}{\partial t} - \frac{\dot{B}_0}{2B_0}\frac{\partial}{\partial \rho}\rho\right)\left(V' n_e\right) + \frac{1}{V'}\frac{\partial}{\partial \rho}\Gamma_e = S_e \\ \frac{3}{2}\left(V'\right)^{-5/3}\left(\frac{\partial}{\partial t} - \frac{\dot{B}_0}{2B_0}\frac{\partial}{\partial \rho}\rho\right)\left[\left(V'\right)^{5/3} n_e T_e\right] + \frac{1}{V'}\frac{\partial}{\partial \rho}\left(q_e + \frac{5}{2}T_e\Gamma_e\right) = P_e \\ \frac{3}{2}\left(V'\right)^{-5/3}\left(\frac{\partial}{\partial t} - \frac{\dot{B}_0}{2B_0}\frac{\partial}{\partial \rho}\rho\right)\left[\left(V'\right)^{5/3} n_i T_i\right] + \frac{1}{V'}\frac{\partial}{\partial \rho}\left(q_i + \frac{5}{2}T_i\Gamma_i\right) = P_i \\ \sigma_{\parallel}\left(\frac{\partial \psi}{\partial t} - \frac{\rho \dot{B}_0}{2B_0}\frac{\partial \psi}{\partial \rho}\right) = \frac{J^2 R_0}{\mu_0 \rho}\frac{\partial}{\partial \rho}\left(\frac{G_2}{J}\frac{\partial \psi}{\partial \rho}\right) - \frac{V'}{2\pi\rho}\left(j_{BS} + j_{CD}\right) \end{cases} \tag{4.1}$$

Here, the space-like variable rho is the label of the flux function, V' stands for $\frac{\partial V}{\partial \rho}$, B_0 is the toroidal magnetic field at the specific radial position, Γ_e the electron flux on the relative magnetic surface, similarly to the ions flux Γ_i. In the last equation, $\sigma_{\parallel}$ is the electrical conductivity, J the plasma current, G_2 a metric coefficient, j_{BS} the bootstrap current, and finally j_{CD} the current driven by external sources. The S_e, P_e, and P_i in the right-hand side of the first three equations are the correspondent source terms of electron particles, electron, and ion power. Specifically, the particle source takes into account all the atomic processes that have been explained in paragraph 2.2 while the powers for ions and electrons are the terms explained in the power balance 2.1. They can be better visualized in the following form, according to [28]:

$$\begin{aligned} S_e &= s_{ion}^{(e)} N n_e + s_{ion}^{(i)} N n_i - s_{\text{rec}}\, n_i n_e \\ P_e &= P_{OH} - P_\Gamma - P_{ei} - P_e^{RAD} - P_e^N + P_e^H + P^{FUS} \\ P_i &= P_\Gamma + P_{ei} + P_i^N + P_i^H \end{aligned} \tag{4.2}$$

where N is the density of neutral atoms, s_{ion} the ionization rate and s_{rec} the recombination rate. In the power balances, it is possible to recognize the positive contributions of the Ohmic and auxiliary heating P_{OH} and P_e^H, mainly affecting electrons, as well as the fusion power P^{FUS}. The negative contributions instead are the heat exchanged in collisions between ions and electrons P_Γ and P_{ei}, that are lost in the balance of electrons and gained in the case of ions. Finally, losses due to radiations P_e^{RAD} and atomic processes P_e^N are considered, as losses for the electrons and gain for ions, to fulfill conservation laws.

An important comment is that ions density is not evaluated by the basic set (4.1) since it will be retrieved by means of quasi-neutrality conditions with electrons and impurities' ions concentration.

The strategy to close the system of equations and get the radial profiles of densities and temperatures is to express fluxes in terms of thermodynamic forces. The concise way to visualize the closing of the system is the matrix problem solved by ASTRA, [28]:

$$\begin{pmatrix} \frac{\Gamma_e}{n_e} \\ \frac{q_e}{n_e T_e} \\ \frac{q_i}{n_i T_i} \\ V' G_1 \frac{\mu_0 j_{BS}}{B_p} \end{pmatrix} = -V' G_1 \begin{pmatrix} D_n & D_e & D_i & D_E \\ \chi_n^e & \chi_e & \chi_i^e & \chi_E^e \\ \chi_n^i & \chi_e^i & \chi_i & \chi_E^i \\ C_n & C_e & C_i & 0 \end{pmatrix} \cdot \begin{pmatrix} \frac{1}{n_e}\frac{\partial n_e}{\partial \rho} \\ \frac{1}{T_e}\frac{\partial T_e}{\partial \rho} \\ \frac{1}{T_i}\frac{\partial T_i}{\partial \rho} \\ \frac{E_\parallel}{B_p} \end{pmatrix} \tag{4.3}$$

where it is possible to distinguish the coefficient matrix, where diffusive and convective coefficients of particles and heat transport (respectively represented by D, C, and χ) are represented.

The requirements to solve the system of partial differential equation 4.1 are the knowledge of transport coefficients, as well as initial and boundary conditions. The first requisite is satisfied by means of specific codes called as modules in the ASTRA main code file. In the framework of this thesis, the diffusive and convective coefficients, both neoclassical and turbulent have been calculated by the respective subroutines NCLASS and TGLF, which will be better explained in the correspondent paragraph (4.1.2). The other two are instead defined by the users, together with the position of the boundary, which should be the *separatrix* (see 4.2).

4.1.1 The STRAHL code

The main job of ASTRA is to calculate radial profiles of kinetic quantities of the main plasma species and of the impurities. When impurities transport has to be analyzed, the STRAHL code can be employed. For the purposes of this thesis, where preliminary studies on the effects of the impurities in the core of EU-DEMO are performed, it has been chosen not to complicate too much the setup of the simulation, already challenging due to the coupling between the other codes, in simulating such a big machine that requires a wider and denser grid. Despite this, in this section the main features of the STRAHL code are described, to depict the relevant upgrade that it could bring to the accuracy of the simulations.

STRAHL [29] in fact, is a code capable of solving the continuity equation in the radial direction for impurities at different ionization stages, giving as output a more accurate solution with respect to ASTRA that consider only the average charge.

Each impurity, depending on its charge, could enter the plasma as fully ionized or with some electrons still not extracted. For low-charge impurities, particles are usually fully ionized and it has been proven that even ASTRA is able to give reliable results, but when heavy impurities, such as Tin, are analyzed, the usage of STRAHL makes results way more precise.

STRAHL solves the following particle conservation law:

$$\frac{\partial n_{I,Z}}{\partial t} = -\nabla\Gamma_{I,Z} + Q_{I,Z} \tag{4.4}$$

where the subscript I stays for the impurity attribute and Z for the ion stage. $\Gamma_{I,Z}$ is the flux of impurities particles and $Q_{I,Z}$ is the sources and sink term accounting for ionization, recombination, and charge exchange effects and has the role of connecting neighboring stages.

While the density distribution $n_{I,Z}$ and the source term $Q_{I,Z}$ are constant on a magnetic surface, the flux $\Gamma_{I,Z}$ presents a poloidal variation and the expansion of its derivative leads to:

$$\frac{\partial n_{I,Z}}{\partial t} = -\frac{1}{r}\frac{\partial}{\partial r} r \left\langle \Gamma_{I,Z} \right\rangle + Q_{I,Z} \tag{4.5}$$

The flux can be written in terms of a diffusive and convective contribution, with correspondent coefficients D and v, which will be then averaged depending on the magnetic surface. The final transport equation to be solved by STRAHL is the one represented in 4.6, where the sum over all ionization stages has been performed so that the only source terms remaining are the ionization and the recombination between neutrals and single ionized ion.

$$\frac{\partial n_I}{\partial t} = \frac{1}{r}\frac{\partial}{\partial r} r \left(D \frac{\partial n_I}{\partial r} - v n_I \right) + Q_{I,1} \tag{4.6}$$

The domain simplification employed by STRAHL follows the same concept as the one of ASTRA, averaging various parameters on the magnetic surfaces, and this makes possible the coupling between the two. Indeed, STRAHL is able to be run in a *stand-alone* configuration, with parameters of background plasma given as experimental values, but the coupling with ASTRA makes it possible to give as input to STRAHL the newly calculated profiles of temperature and density of each ASTRA iteration, as well as the transport coefficients, and, in turns, to use the accurate result of impurity distribution of STRAHL to update the background profiles themselves. The tightly two-way coupling of ASTRA and STRAHL, together with the other two codes TGLF and NCLASS in the newly innovated version of ASTRA is still ongoing by the team of astra developers.

4.1.2 TGLF and NCLASS codes

The TGLF (Trapped-Gyro-Landau-Fluid) code [30], is capable of evaluating the turbulent fluxes of particles and heat, accounting for the micro-turbulence effects of both circulating and trapped particles in a fast and accurate approximation. Before TGLF, only the Gyro-Landau-Fluid equations were considered in the study of turbulence inside the plasma, deriving from the velocity moments of the gyro-kinetic equation and considering only linear effects like the Landau damping - an exchange of energy between particles and waves drifts generated by instabilities, leading to exponential damping of the energy of the instability - [31]. With the development of studies on turbulence, trying to account for micro-turbulences like the ETG, ITG, and TEM modes, previously described in section 3.3, the need for describing non-linear phenomena also for trapped particles, which are the ones giving more contribution to transport, aroused.

The TGLF code is able to calculate with a *quasi-linear* approximation the perturbation and the amplitude of these instabilities (from here the *quasi-linear* approach), considering both circulating and trapped particles, resulting in a validated model for the turbulence effects in Tokamaks.

The output of TGLF is the total turbulent flux, from which is it possible to evaluate the turbulent transport coefficients both of the background plasma and of impurities used in the simulation.

NCLASS [32] is the code responsible for calculating the neoclassical fluxes in different collisional regimes solving the radial and parallel force balance within a magnetic surface.
The code returns the particle flux which takes into account, in five different components, the effects of banana-plateau flux driven respectively by pressure and temperature forces, parallel electric field forces, and external forces, as well as Pfirsch-Schlüter and classical fluxes. Also, convective pinch and effects related to temperature and pressure gradients are part of the phenomena considered by the numerical solution, together with conductive heat fluxes which lead to the calculation of thermal transport coefficients (χ). The capability of considering all these pieces of physics makes this code very attractive, being comprehensive of several neoclassical (and classical) effects.

Both codes are called in ASTRA to calculate the diffusive and convective coefficients for particles and heat, then used for solving the system of equations reported in 4.3 to get density and temperature profiles of the main plasma, but also the density distribution of impurities, once these coefficients are given as input to the STRAHL code, which solves the correspondent equation 4.6.
The method used to couple and interface these codes will be better described in the specific paragraph on the setup of the simulation 5.1.

4.2 Coupling strategy with SOLPS-ITER code

This section focuses on the strategy used to initialize the process of coupling the two codes ASTRA and SOLPS-ITER, to achieve the great ambition of integrated modelling the transport of particles across the two very different regions of SOL and core.

First of all few words must be spent regarding the SOLPS-ITER code. It solves the 2D transport problem of magnetized plasma in the SOL region, assuming toroidal symmetry and accounting for the relevant transport phenomena both along and across field lines (see 2.1).
As described in section 2.2 in fact, in the SOL region atomic processes lead to important mechanisms of exchange of energy and momentum between neutral particles and partially-ionized species. The SOLPS-ITER code has a specific module devoted to solving Braginskii-like multi-fluid equations, approximating as a single fluid each charge state of the species, and another module that instead solves the kinetic equation for neutral particles. The latter task is performed by the EIRENE code, using Monte Carlo methods [33].

The main idea behind this first try of *one-way coupling*, consists in taking the

output of SOLPS-ITER and using it as input for the ASTRA code. A further step will be comparing the output of the core simulations with the initial condition given by SOLPS-ITER and adjusting results in an iterative procedure.
In particular, the parameters reported in the table have been used, being the output of simulation performed with SOLPS-ITER code on the same EU-DEMO scenario and having reached steady-state conditions.

Parameter	
R_0	7.5 $[m]$
a	3.3 $[m]$
a_{wall}	3.7 $[m]$
I_{pl}	19.07 $[MA]$
B_{tor}	4.89 $[T]$
$\Gamma_{imp,sep}$	$\sim$
$n_{DO,sep}$	$\sim$
q_{prof}	fig (4.2)

Table 4.1: Parameters used as input for ASTRA, representing the output of the SOLPS-ITER simulations. The values of $\Gamma_{imp,sep}$ and $n_{DO,sep}$ are different for the Lithium and Tin case, and will be specified in the results' sections 5.2.2, **??**.

In the following figures 4.1 and 4.2 are reported respectively the poloidal section of the plasma domain where the separatrix and the wall are depicted, and the safety factor profile of the scenario under study.

The separatrix represents the boundary between the two different regions of core and SOL, which needs further clarification regarding its use as boundary location between the two codes calculations.
Using the separatrix as the boundary between the two codes would have been the most accurate solution since the last closed magnetic field line divides the two distinct regions with different transport mechanisms. However, from the separatrix going to the core, exist an area called *pedestal* in which strong gradients of density and temperature usually occur, especially in the so-called *H-mode* [34].
In this zone, turbulence and not yet described in a satisfactory way effects, arise, and the ASTRA code is not able to describe accurately the transport. Hence, the location at which the core transport starts to be modeled is a bit further inside the separatrix, specifically at $\rho = 0.85$, neglecting the effects of the pedestal. Further development of this work could focus on a scan of the position of the boundary and considering some effects of the pedestal studying the sensibility of the issue.

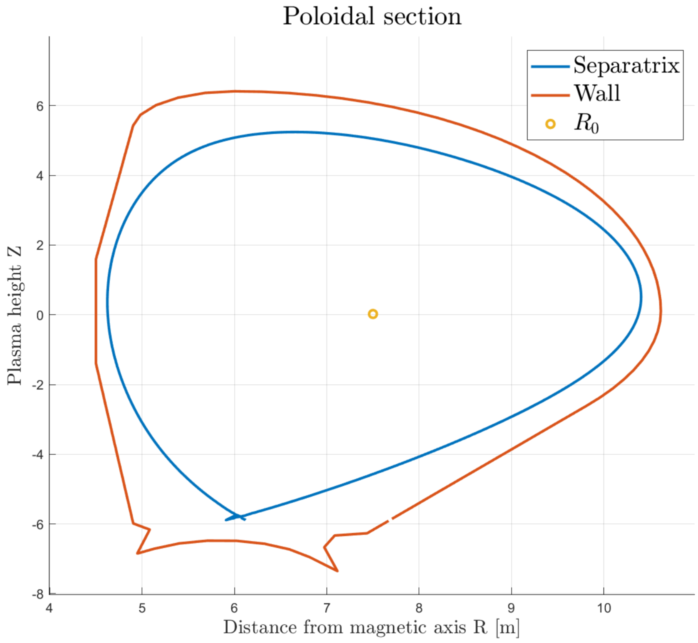

Figure 4.1: Sketch of the geometrical configuration of plasma boundary and location of the wall in a poloidal section.

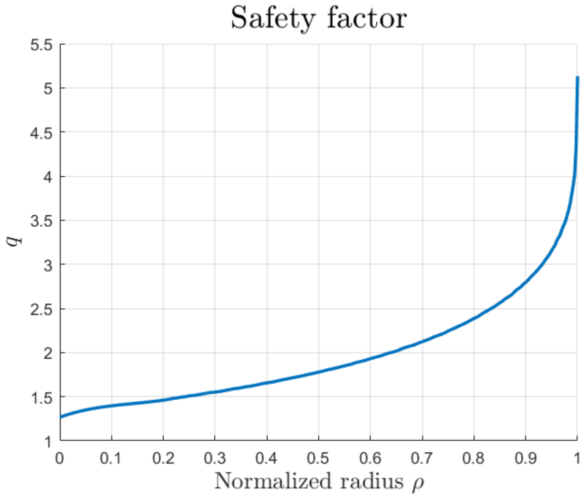

Figure 4.2: Graph of the safety factor profile across the normalized radius ρ.

Chapter 5

Setup of simulations and results

5.1 Setup of the simulations

The strategy with which the *direct coupling* between SOLPS-ITER and ASTRA code is implemented is schematically described in figure 5.1.

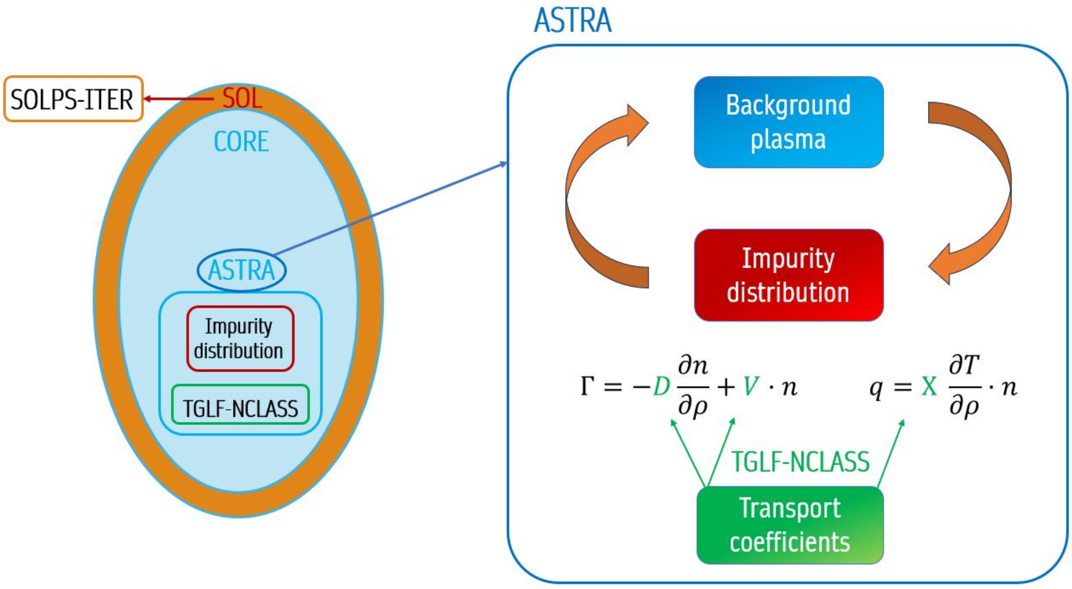

Figure 5.1: Schematic representation of the whole coupling strategy.

Specifically, the output of the SOLPS-ITER calculations (coupled with a model for the temperature of the target [35]) are given as input to the ASTRA code. In the latter, an *auxiliary function* is used in order to calculate the distribution of the impurity. For solving the background plasma and impurity parameters, transport coefficients of particles and heat are needed, and they are evaluated by NCLASS and TGLF, respectively for the neoclassical and turbulent cases. At each iteration, the background plasma is evolved and calculated by ASTRA, then the distribution of the impurity is calculated and influences back the ion density by means of quasi-neutrality condition.

In the following paragraphs, a focus on how to define the physical model and the characteristics of the reactor to ASTRA is now addressed, describing its main repository structure.
The fundamental files in which all the information is given, are the *model file* and the *experimental* one. In the former, the formulation of the transport problem, specifying the species in terms of chemical and physical properties, is contained, as well as the selection of the way in which to visualize and extract the results of the simulation. In the latter instead, the geometrical dimensions of the reactor and the initial and boundary conditions are set: these can be experimental values or simply defined by the user.
The main sections of the *model file* will be described, presenting some interesting examples to compare with the physics explained in the initial chapters.

- **Plasma species**
  This section contains the definition of the mass and charge of each species in the model, both of the main plasma and of the impurity. Then, also the condition of quasi-neutrality is here imposed, and reported in the following:

  ```
  NMAIN = NDEUT+NTRIT;
  NDEUT = 0.5*(NE-ZIM1*NIZ1);
  NTRIT = NDEUT;
  NI = NDEUT+NTRIT+NIZ1;
  ```

  where `N` stays for the density of the different species, and the subscripts `DEUT` and `TRIT` represent respectively the deuterium and tritium species, as well as `NI` and `NE` stands for ions and electrons and `NMAIN` for the main plasma. Finally, `ZIM1` and `NIZ1` are namely the average charge and the density of the impurity that we are considering. If we substitute the values of `NDEUT` and `NTRIT` in `NMAIN` it is possible to recognize the condition of quasi-neutrality since the ion concentration of deuterium is half of the number of electrons to which the electrons of the impurities in their charge state is subtracted and the other half is given by the same value corresponding to the concentration of tritium. Finally, the ion concentration `NI` considers all the ions present in the plasma.

The calculation of the parameter `ZIM1` (as well as the `PRAD` that will be described in the following section) has been possible through the implementation of brand-new functions in the libraries of ASTRA. These have been written during the development of this thesis and added to the standard libraries of ASTRA where formulas which define the *average charge* and *cooling rate functions* for different species at different temperatures in the *coronal equilibrium* are present.
In fact, as described in the paragraph 3.4, the value of the average charge and the correspondent radiated power, depends on the temperature of the plasma as well as the dwell time, hence the condition of coronal equilibrium or not. Using atomic data tabulated in the OPEN-ADAS (Atomic Data and Analysis Structure) dataset [36], it has been possible to implement L_Z and $< Z >$ functions in coronal equilibrium at different temperatures both for Lithium and Tin, so that the average charge of the impurity and the correspondent radiated power has been calculated. As stated, considering functions at coronal equilibrium means neglecting transport effects, as the impurity particles move very fast. This approach is enough accurate for the Lithium case since with its low number of electrons, very easily becomes fully ionized and both the average charge and the radiated power assume almost coronal equilibrium.
This could be slightly different for the case of Tin, which instead has a higher charge, and depending on the ionization stage, of course, the average charge but also the cooling rate function will be different.
Formulas written for the Lithium and Tin case are reported in Appendix A A.

For the purposes of this thesis, impurity species have been assumed to be in coronal equilibrium, but further improvements, for example using STRAHL code or Aurora, which are able to evaluate the distribution of impurities at each ionization stage, can be done.

- **Sources**
  In this section, sources of particles and of power are defined. Specifically, for the case of this thesis, the concentration of cold neutrals particles of deuterium is specified, taking the value from the SOLPS-ITER simulations, and then used by ASTRA to calculate the neutral density and distribution, as well as the source of particles due to ionization and recombination effects. Then, the auxiliary power coming from the ECRH (Electron Cyclotron Resonance Heating) is set, with a Gaussian shape localized in the magnetic axis and a peak value of 50 MW. This power is going to increase the kinetic energy only

of the electrons, resonating with their gyro-frequency and leading to a very effective extra-heating mechanism that should help to maintain the fusion power to the values required by the EU-DEMO scenario. Finally, the power balance is set, and it can be possible to compare the formulation with 4.2.

```
PE=PEBM+PEECR-PEICL-PRAD+PEDT;
PI=PIBM+PEICL+PIDT;
```

The various components of the electron power are respectively the Bremsstrahlung radiation of electrons, the ECRH power, the collision term between ions and electrons, the radiated power, and the power of fusion released by electrons and ions. For the ion power balance instead, on the right-hand side, the Bremsstrahlung radiation for ions, the term due to collision, and the power produced by fusion are all source terms.
As previously foretold, the formula to calculate the radiated power for both Lithium and Tin has been added. In particular, it has the form of 3.15 and the function of the total cooling rate L_z has been implemented starting from tabulated values of OPEN-ADAS and accordingly to ASTRA units, used in the *model file* in the following way (i.e. for the case of tin):

```
PRAD = PSYNC + PBRAD + PRTIN*NE*NIZ1;
```

The function implemented for the specific impurity is simply the `PRTIN`, and it is then multiplied by the electron and impurity density following 3.15, and also the power radiated by electrons' synchrotron and Bremsstrahlung radiations have been added, calculated by ASTRA *built-in* functions `PSYNC` and `PBRAD`.

- **Transport models**

  In this section, the transport coefficients of the background plasma and of the impurities are evaluated, together with some other parameters which are needed to define the transport model that describes the plasma condition. In fact, as explained in the section 3.2, depending on the collisionality regime, the dominating transport effects will be completely different. Hence, the calculation of transport coefficients of heat and particles is fundamental to define which kind of transport, between turbulent or neoclassical, prevails, defining the collisional regime.

- **Transport equations** This section contains the line of code in which the main plasma quantities are calculated. In particular, ASTRA evolves the electrons' density, the electrons' and ions' temperature, and the plasma current in the radial direction as explained in the section 4.1 with the system of equations 4.1. In ASTRA is it possible to evaluate the evolution in time of these parameters, or to maintain them constant and assigned to the initial value. For the purposes of this thesis, the first three mentioned parameters have been evolved, to see if the fusion power (influenced both by temperatures and density) is maintained at a high enough value to sustain the reaction, whereas the current, that is the one related to the safety factor profile, has been kept constant. This is the moment in which initial and boundary conditions have to be defined, and it can be better understood how to do it by looking at the lines in which the electrons' density profile is made evolved:

```
NE=NEX;
NE:EQ[2,CBND1];
NEB=NEX(AFX(CBND1));
```

The first line represents the initial condition, which is taken by the *experimental file*, where the initial profile is set according to the generic EU-DEMO scenario under study, which is described in [37] and from where also the initial electrons and ions temperature distribution has been taken. They are also reported in figure 5.2.

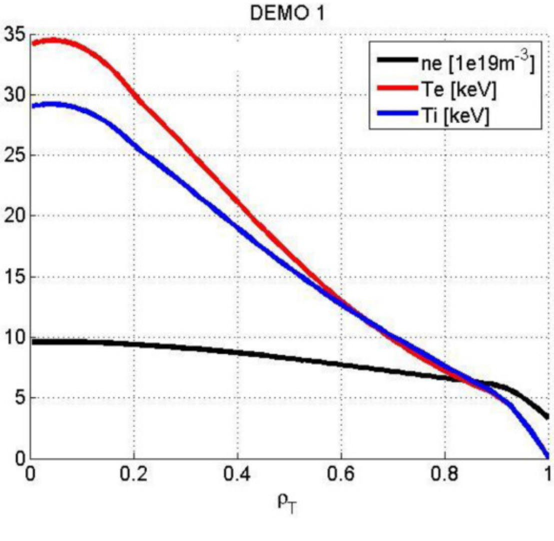

Figure 5.2: Density and temperature profiles calculated with ASTRA for DEMO 2018 [37].

The second line is the command in the ASTRA language that calculates the evolution of the electron density, depicted from the `NE:EQ[Tag,Expr1]` string.

It means that the transport equation for the electron density is evolved. Inside the squared brackets, the right boundary of the transport equation is defined in `Expr1`, which for the case of the simulation is defined by the constant value `CBND1 = 0.85`. The `Tag` represents the type of the radial coordinate that is used to express the boundary condition, and in this case, the value `2` means that dimensionless coordinates are used, namely $\rho_N = \rho/\rho_B$ where ρ_B is the dimension of the minor radius of the plasma.
Finally, the last line assigns the boundary condition value to the density distribution, which is defined by the experimental profile in the location `AFX(CBND1)` that is simply the value that the experimental value of the electron density assumes at the boundary location.

The same thing has been done for the *auxiliary function* that calculates the impurity density distribution:

```
DF1 = CAR41;
VF1 = CAR43;

F1 = 1.e-4*NE;
F1:EQ[2,1.d0];
F1B=3.45e-3;
```

where the last three lines represent the same condition explained for the main plasma, while the first two are the definition of the diffusive and convective transport coefficients used for the solving of the `F1` equation and containing both the neoclassical and turbulent contributions.

An important comment that has to be done at this point regards the location of the boundary condition. For the simulations performed for this work, the boundary has been put at 0.85, limiting the ASTRA calculation inside the core, and maintaining constant profiles in the pedestal region. In the perspective of enhancing this work, a scan of the location of the boundary could be done, to study the sensitivity of the model with respect to the anomalous effects that occur inside this region.

- **Plotting radial profiles**

  The final section of the *model file* is devoted to the lines for the visualization of results. The ASTRA code is equipped with a graphical window, with which is it possible to control the evolution of the simulation and interactively do

variation of parameters.
An example of visualization of data is here reported, showing the lines of code that have been written in order to visualize the correspondent parameter in the ASTRA graphic window 5.3.

```
!------- plotting radial profiles --------!

! Page 1: main profiles and transport
! top panel, red
Te\TE\\TEX\-3;  Ne\NE\\NEX\-13;  Prad\PRAD;  Pfu\CAR15;
! lower panel, red
Chie\HE\-5;    De\DN;   Dz1\CAR41\10.;   Dtur\CAR27\10.;
! top panel, blue
Ti\TI\\TIX\-3;  Ni\NI\-13;  Vz1\VF1\10.;  Vtur\CAR28\10.;
!lower panel, blue
Chii\XI\-5;  Vce\CN + 10.;  NzA\F1\-8; PEC\PEECR;
cf5_CF5; pfus_QDTB*5.;
```

In the graphic window, it is possible to follow the evolution of the various parameters that have been visualized, having the possibility of changing different physical or simple graphic display parameters with the buttons on the lower side of the window. Also, in the upper line, the machine (`dem-`), the shot number (of course arbitrarily in this case), and the other main geometrical and physical parameters are reported, together with the time reached by the plasma shot and the time interval between any ASTRA iteration (calculation of equilibrium and evolution of transport). A clarification that has to be done is that the code is not able to stop if the condition of fusion is not anymore fulfilled or if any other properties or instabilities make physically the plasma shut down, so it is the duty of the user to understand at what time the plasma, given the condition depicted by the simulation, will stop to exist, even if the simulation continues to run.

Once the *model file* and the other input files are set, the simulation is ready to be launched, and the user is able to check the convergence of some specific parameter in the same graphical window previously explained. When they are satisfied with the reaching of a steady-state regime the output of the simulation, saved in ASCII characters, is then converted into numerical tables by the `A2CDF` subroutine. At this point, the results have been imported into a Python script, where all the radial and temporal evolution of each parameter are post-processed. Simulations performed for this thesis work have reached convergence after 10 seconds of simulation time, which takes around 7 hours to run.

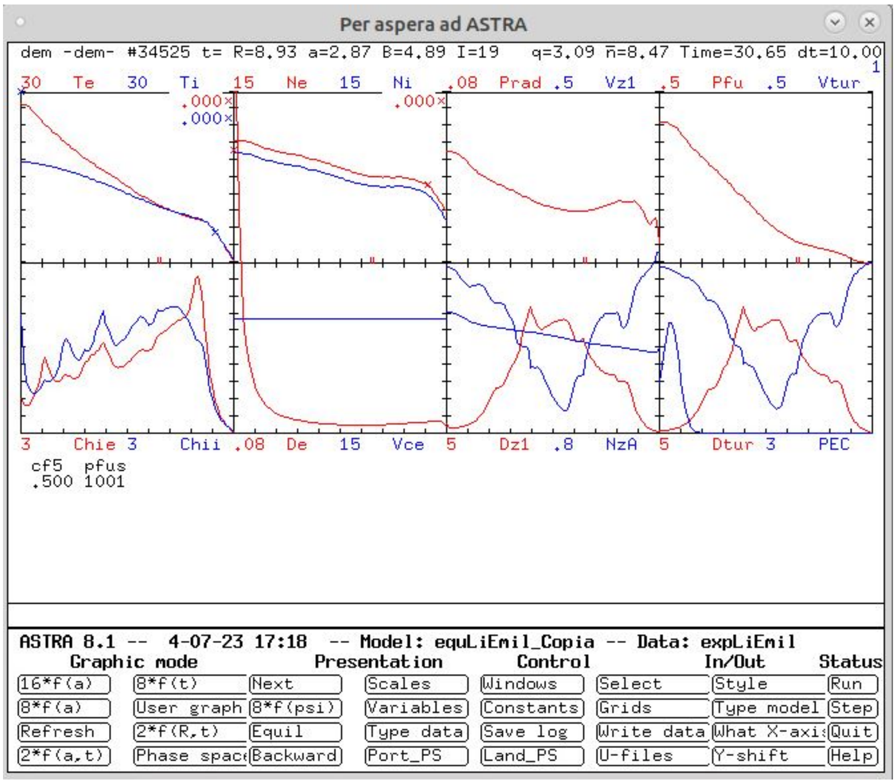

Figure 5.3: Example of the ASTRA interactive graphic window of a generic shot.

5.2 Results

In the following paragraph, the results of the simulations for Lithium and Tin are presented. In particular, a scan of the source of impurity entering the core has been made, for the two cases. For each impurity two different situations have been considered, one with a higher and one with lower values of the impurity source, taking the output of SOLPS-ITER simulations [35]. The scenario with the lower source represents the realistic situation in which also Argon has been injected into the edge plasma, to make it radiate and allowing to decrease the amount of Lithium or Tin needed to reach affordable values of radiation at the edge. In fact, the *Argon seeding* is a very common technique used in fusion machines in order to decrease the temperature at the edge, being Argon a light impurity with a high value of radiative cooling rate (see fig. 3.8), hence being very effective in radiating without reaching and polluting the core. For this preliminary work, it has been considered only the presence of Lithium or Tin inside the core as impurity species, assuming reasonably that the Argon will not reach the core affecting its power and particle balance. Nevertheless, the source of the two impurities has been taken coherently

lower and the results studied.
Firstly, the reference scenario for EU-DEMO without the presence of any source of impurities is presented, showing the radial profiles of the main plasma parameters. This will be then compared with the resulting profiles obtained with the presence of Lithium and Tin, looking at what are the most affected parameters and the resulting impact in terms of fusion power and plasma dilution.

5.2.1 Reference scenario without impurities

The reference scenario from which the analysis starts is the situation in which no impurities are considered to be present inside the reactor. Hence, a simple simulation has been done with ASTRA in order to define the starting condition of the reactor, to be then able to compare coherently the effects of the presence of impurities like Lithium and Tin.
In the following, the ion and electron temperatures (5.4), as well as the density (5.5) are shown.

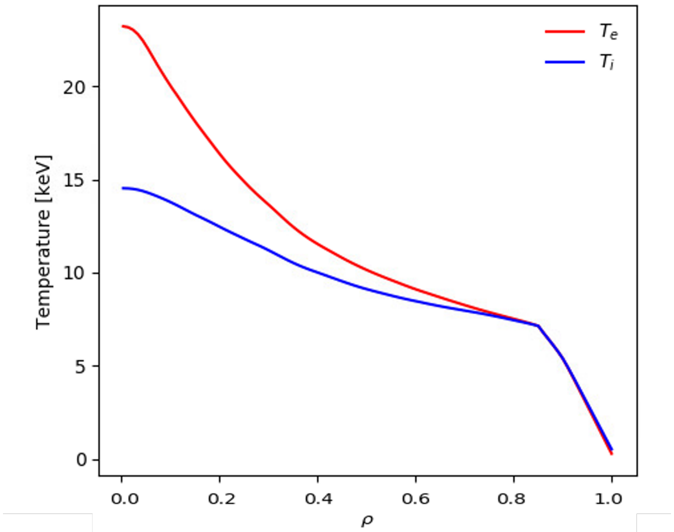

Figure 5.4: Electron and ion temperature for the reference scenario in the radial direction

It is also important to show the value of fusion power that is reached in this condition to complete the set of parameters that will be compared. In figure 5.6, the fusion power produced by the plasma with the above-represented conditions of temperature and density is reported, together with the value of power radiated by electrons due to synchrotron and Bremsstrahlung radiations. Integrating the value of fusion power all across the entire volume of the EU-DEMO reactor gives

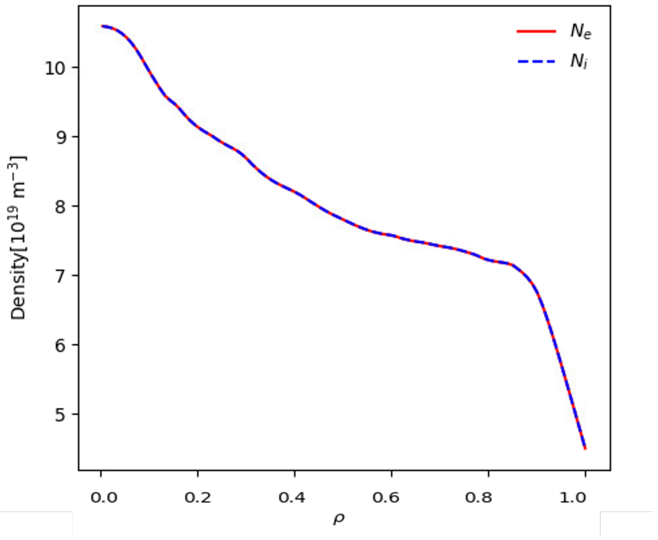

Figure 5.5: Electron and ion density for the reference scenario

us the rate of fusion power produced by this scenario. Using an ASTRA function which performs the actual integral of the fusion power density over the core plasma volume, the corresponding rate of power amounts to $\sim 800[MW]$. This value is less than half of the required by the EU-DEMO scenario obtained by [37] for example, in which the aimed fusion power rate should be around $2[GW]$. This is consistent with the fact that results obtained by the reference scenario simulation considered in this thesis have a lower temperature in the core with respect to the scenario of [37]. Nevertheless, this scenario does produce fusion energy, that anyway, should results be taken quantitatively, would not be sufficient to prove the feasibility EU DEMO-like approach as a future means electricity generation.

This is deemed not to be a severe issue in terms of the objective of this thesis, which is aimed at qualitatively comparing conditions without or with impurities. Future work will be devoted to a deeper analysis of the power balance for ions and electrons to identify the cause of the temperature decrease and of the consequent reduction of fusion power, in order to draw more quantitative conclusions.

From now on these graphs will be the reference ones for all the comments on scenarios in which Lithium or Tin are used as liquid metals in the divertor.

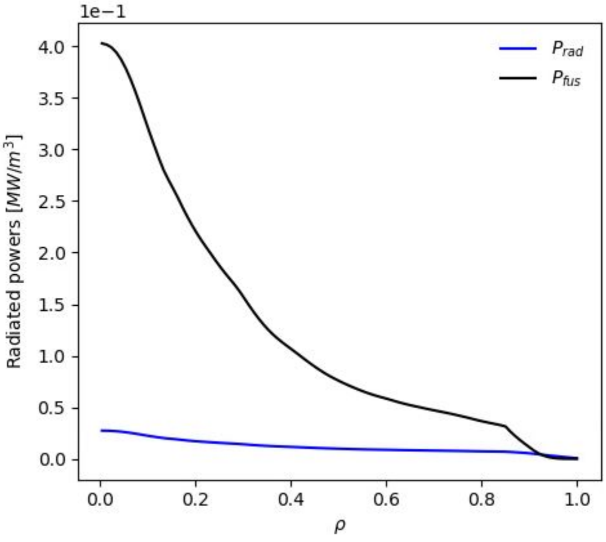

Figure 5.6: Fusion power density and radiated power density by electrons for the reference scenario

5.2.2 Lithium

In this section the analysis of the simulations which represent the scenario that uses Lithium as liquid metal is performed, focusing on main engineering parameters and on interesting plasma profiles.
As previously stated, the two cases under study, consider two different values of source term for the impurity entering the core from the edge (n_{imp}). These values, schematically represented in figure 5.7 are set as a boundary condition for the evolution of the impurity density distribution (see par. 5.1) and it is the only difference considered between the two simulations.

In figure 5.7, the horizontal dashed line represents the limit in the percentage of Lithium density with respect to the electron one at the separatrix, that was estimated to be allowable in a reactor to achieve sufficient fusion performance, according to [38]. For the Lithium case, it amounts to 3% and what is expected is that the fusion power in the core decreases that much not to make fusion itself self-sustaining due to a big accumulation of Lithium for the first case in which the Lithium source term is higher, differently to what will happen for the second case. Two separate sections for the results of each simulation will be now presented.

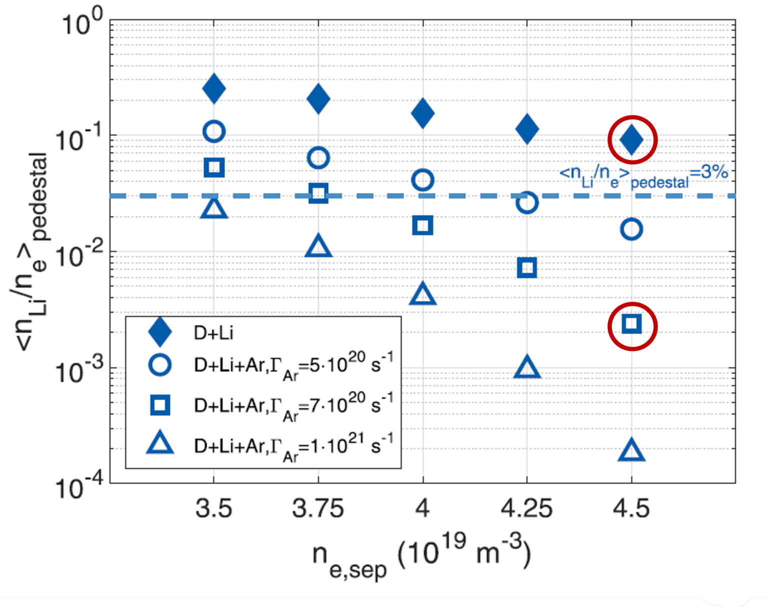

Figure 5.7: Plot representing different scenarios of impurity taken into consideration in the work of [35]. The two cases taken into account in this work are the ones highlighted by red circles.

- **Case 1 -** $n_{Li} = 3.97 \cdot 10^{18}\ [\frac{part}{m^3}]$

  This case represents the results obtained with a higher source of Lithium in the core, according to the higher value circled in the figure 5.7 and equals to $3.97 \cdot 10^{18}[\frac{part}{m^3}]$. In the following table, the main average / integral parameters of engineering interest (thereafter referred to as “engineering parameters” for the sake of simplicity) are shown, representing radially averaged values, and they will be explained afterward.

Case 1	
$\langle P_{fus} \rangle$	766 $[MW]$
$\langle C_Z \rangle$	5%
$\langle Z_{eff} \rangle$	1.35 [-]
$\langle T_e \rangle$	15 [keV]
$\langle T_i \rangle$	10 [keV]
$\langle n_{Li} \rangle$	$3.8 \cdot 10^{18} [\frac{part}{m^3}]$
$\langle n_e \rangle$	$7 \cdot 10^{19} [\frac{part}{m^3}]$
$\langle n_i \rangle$	$5 \cdot 10^{19} [\frac{part}{m^3}]$

Table 5.1: Table of interesting engineering values corresponding to the simulation with a source of Lithium equal to $n_{Li} = 3.8 \cdot 10^{18} [\frac{part}{m^3}]$

As expected, the value of average fusion power (evaluated as a volumetric integral over the torus) reaches a value way lower than the one of the reference case (**??**). This condition is explained by the very high accumulation of Lithium in the core, depicted by the value of $\langle C_Z \rangle$, which is simply the ratio between the impurity density and the electron one, which according to the ASTRA simulation, amounts to 5%. Coherently the average effective charge is equal to 1.35, depicting a polluted plasma (value of Z_{eff} (3.18) equal to 1 represents a pure deuterium-tritium plasma).
It is also possible to notice how much the average electron and ion temperatures have decreased with respect to the reference scenario, due to the accumulation of Lithium in the core, with an average value of $3.8 \cdot 10^{18} [\frac{part}{m^3}]$. This has led to a *dilution* of the plasma, noticeable by looking at the great difference between ions' and electrons' density.
Radial profiles of some of these parameters are now presented, as well as the density distribution of the impurity and of the main plasma.

Firstly, temperature profiles of the main plasma are reported, compared with the fusion and radiated power (5.8). From now on, the radiated power (P_{rad}) represents the sum of radiations due to both electron (comprising synchrotron and Bremsstrahlung ones), and the impurity radiations, comprehensive of both Bremsstrahlung and line radiations, which is instead always represented by the dashed red line.

It can be noticed that the decrease of fusion power with respect to the reference scenario seems to be driven neither by the excessive decrease of temperature nor by the big radiation of the impurity, as expected. In fact, Lithium, being a light impurity, does not radiate that much, as it has been seen in the chapter 3.4 and in the figure 3.8 comparing the radiative cooling rates of different

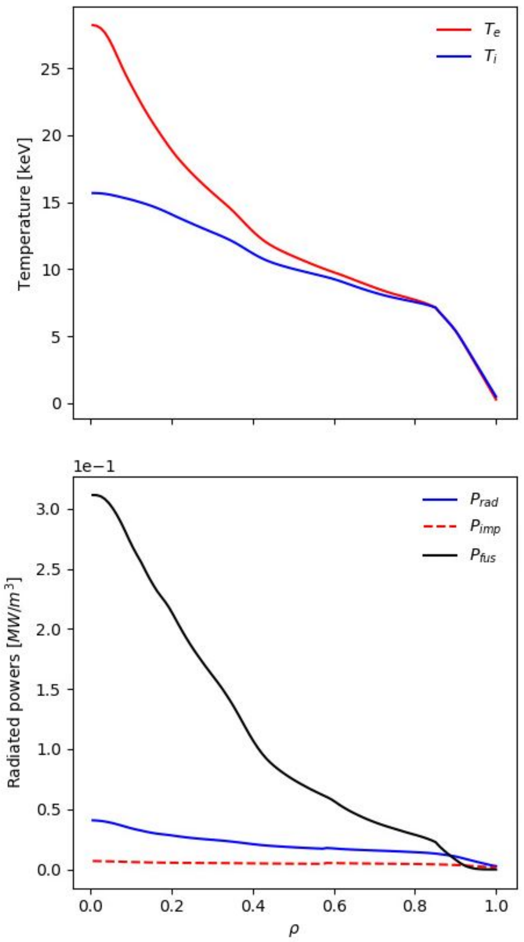

Figure 5.8: In the top plot, the electron and ion temperature is represented, together with the fusion power profile in black, and the total radiated power in blue in the bottom graph. The red dashed line is the power radiated by the impurity.

species. In particular, if a focus is done on the total radiated power and on the impurity radiation by looking at the blue and red dashed line in figure 5.8, it can be seen how the majority of radiation is due to the electrons. Moreover, remembering the different contribution of line radiation and of Bremsstrahlung with the increase of temperature (see fig. 3.9), it can be realized that the showed case is located in the range of temperature in which actually only Bremsshtralung radiation is present, being the impurity fully ionized at that temperature and consequently not allowing line radiation.

Is instead more evident how the decrease in fusion power, is led by the dilution provoked by the impurity accumulation. Indeed, looking at figure 5.9, it is possible to see the decrease in the ions density of the main plasma, due to the impurity accumulation. Since the quasi-neutrality condition is imposed in the model, if a relevant amount of impurity accumulates in the core plasma, the main ions have to decrease.

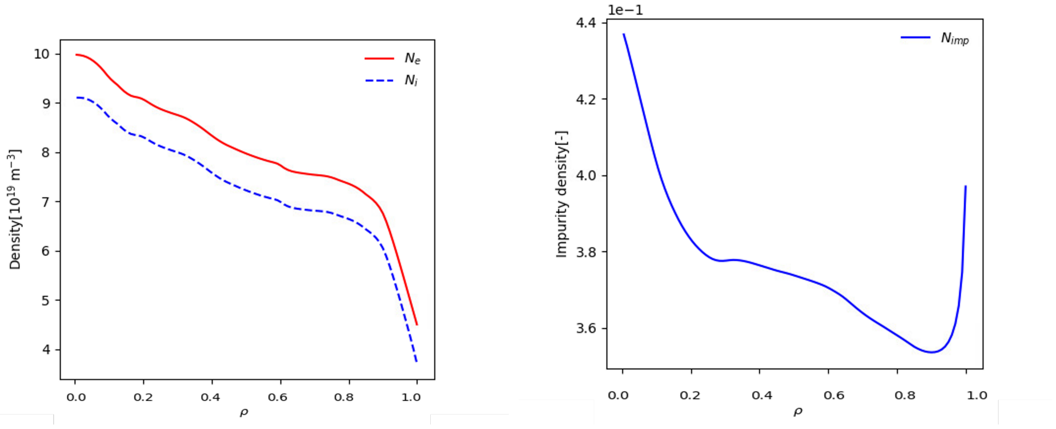

Figure 5.9: On the left-hand side, electron and ion density of the plasma are reported, whereas on the right-hand side impurity density distribution is shown.

Final comments have to be done on the transport processes and the distributions of background plasma and impurities. As explained in chapter 3, turbulent and neoclassical particle transport coefficients regulate the final distribution of species.
By looking at figure 5.10, main plasma and impurity distributions are again shown, this time together with the corresponding transport coefficients.

Focusing on the left-hand graph, representing the background plasma, it is possible to see how the values of transport coefficients are very low and almost not affecting the motion of main particles in the radial direction, which remains practically the same as the initial condition. For the case of Lithium instead, values of coefficients are slightly higher. Both lines represent the total diffusive and convective coefficients, accounting for neoclassical and turbulent effects. It is possible to notice that diffusion gives a higher contribution to the motion of particles, being bigger than the pinch velocity, and most of all positive. This will explain the accumulation of particles on the outer side of the plasma, while the peaked profile in the center is more difficult to explain. In fact, it was expected that the convective coefficient got higher absolute values, leading to an inward pinch in the case it would have gotten a negative value or outward in the opposite situation. The discrepancy could be explained by the complex structure of the coupling between all the codes used in the

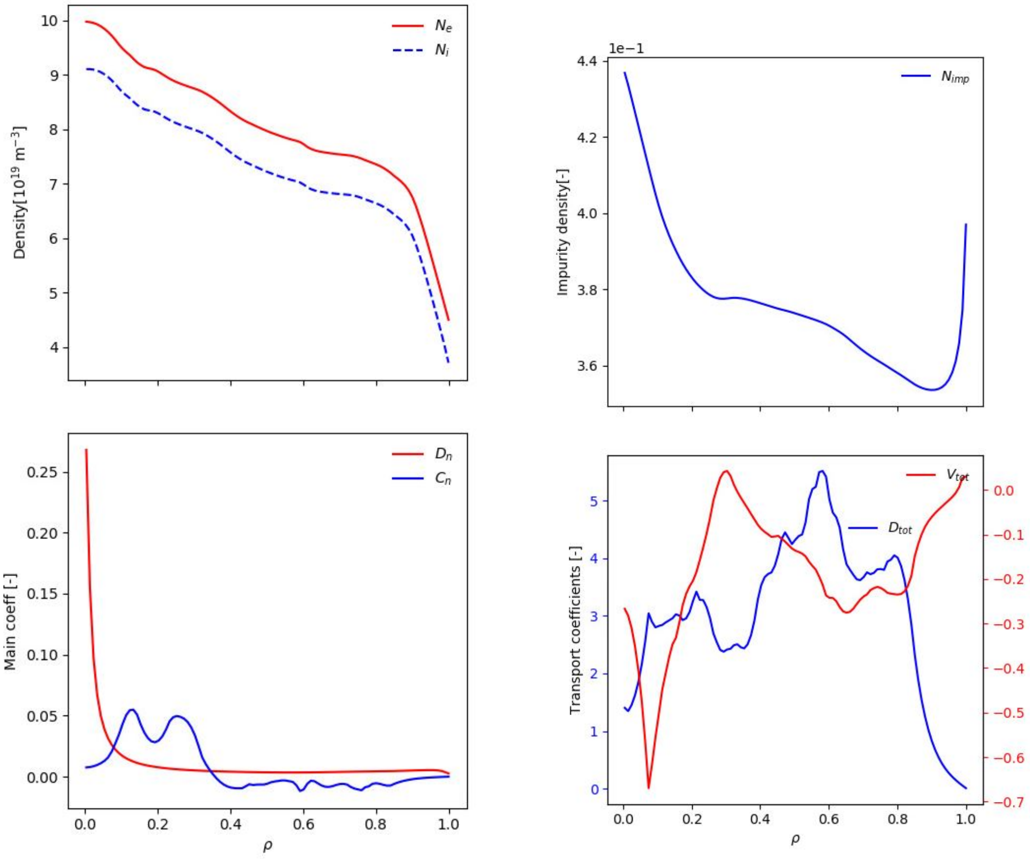

Figure 5.10: Electron and ion density distribution and impurity distribution, together with the corresponding particle transport coefficients at the bottom are reported, respectively on the left and right-hand side of the figure.

simulations, and the resolution grid used. Those fluctuations that are shown in the right-bottom graph are representative of some numerical instabilities that should not describe a real physical effect, surely the focus of future works.

- **Case 2** - $n_{Li} = 1.1 \cdot 10^{17}$ $[\frac{part}{m^3}]$

This case represents the results with a lower source of Lithium, obtained thanks to the injection of Argon to produce the required decreased temperature but with the lower risk of polluting and diluting the plasma.

As in the previous case, the results of engineering parameters are reported in the table 5.1, and then also the radial profiles are plotted, showing the relevant differences with respect to the previous case.

Case 2	
$\langle P_{fus} \rangle$	800 $[MW]$
$\langle C_Z \rangle$	0.3%
$\langle Z_{eff} \rangle$	1.01 [-]
$\langle T_e \rangle$	15 [keV]
$\langle T_i \rangle$	10 [keV]
$\langle n_{Li} \rangle$	$1.2 \cdot 10^{17}[\frac{part}{m^3}]$
$\langle n_e \rangle$	$7 \cdot 10^{19}[\frac{part}{m^3}]$
$\langle n_i \rangle$	$7 \cdot 10^{19}[\frac{part}{m^3}]$

Table 5.2: Table of interesting engineering values corresponding to the simulation with a source of Lithium equal to $n_{Li} = 1.1 \cdot 10^{17}[\frac{part}{m^3}]$

Looking at the table it is possible to realize that the fusion power is very similar to the reference case, as expected. This was foreseen by the simulations performed with SOLPS-ITER, summarized in figure 5.7, which however could not provide any information regarding the impurity distribution in the core. This was also foreseen by the prediction of [38], considering a case in which the source of impurity is really low. Temperatures are almost the same, while the accumulation of impurity has one order of magnitude lower than in case 1. In turn, this lead to a lower dilution of the plasma, which is practically absent as can be seen in figure 5.11 on the upper-left graph.

The radial profiles of main plasma parameters are now shown, stressing the same comments as before on the transport coefficients, which coherently lead the impurity particles on the inner region, and maintain instead almost constant the main plasma density profile.

Finally, looking at the power profiles 5.12 it is possible to see the increase of fusion power with respect to case 1, as expected.

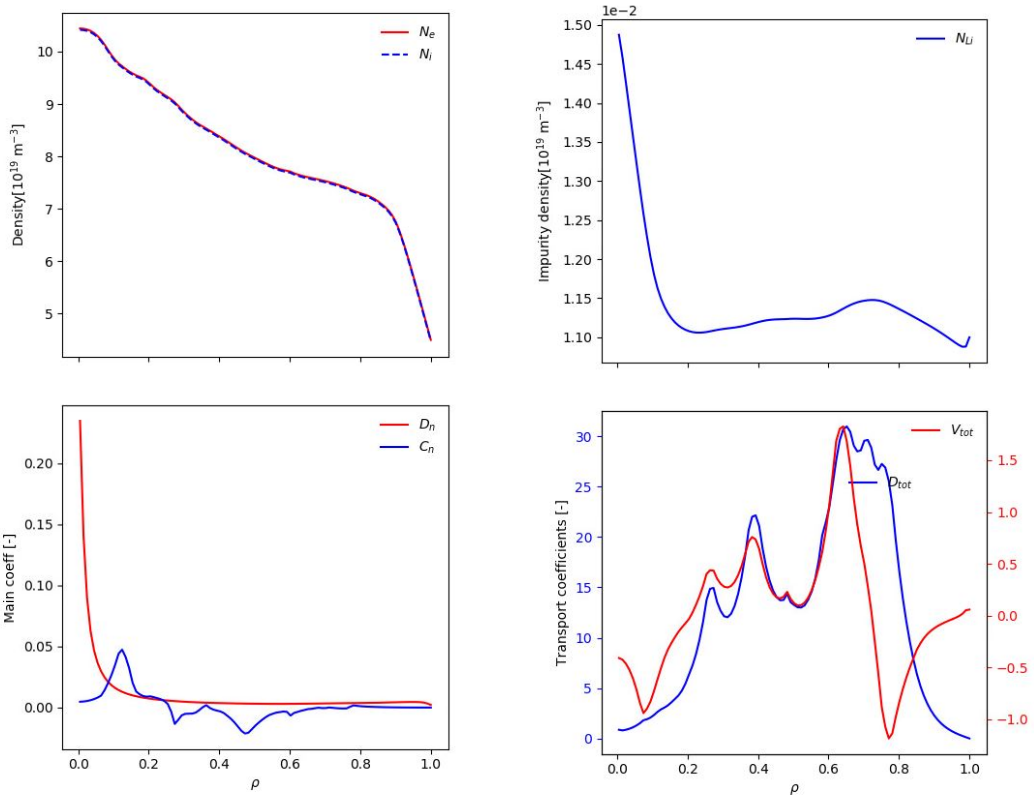

Figure 5.11: On the left-hand side main plasma density and transport coefficients are reported. On the right-hand side the correspondent for Lithium.

5.2.3 Tin

In the following paragraph, the results of the Tin simulations are presented, again for the two cases, which have been taken from the work of [35] and schematically represented in the sketch below 5.13.

As in the case of Lithium, the dashed line represents the maximum concentration allowable according to [38], to get a fusion condition. Hence, it is expected that also in this case the first scenario (with a higher value of Tin source) will generate less fusion than the reference scenario, opposite to the second one.
Again the two cases differ only on the source value of Tin entering the core, and their analysis will be split into two sections.

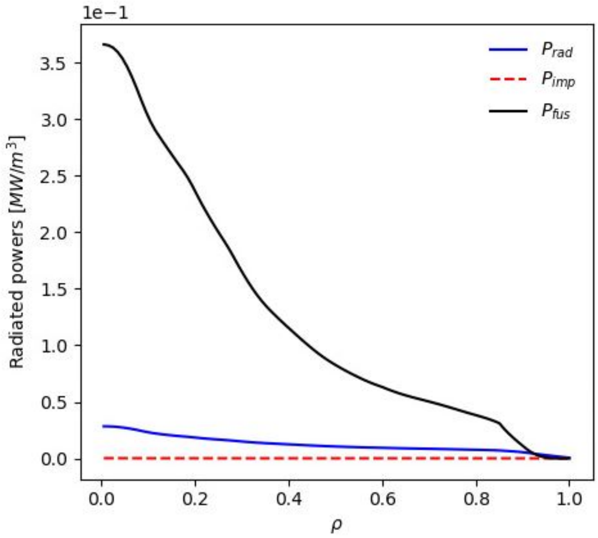

Figure 5.12: The figure represents the temperatures profiles of the main plasma and the fusion and radiated power.

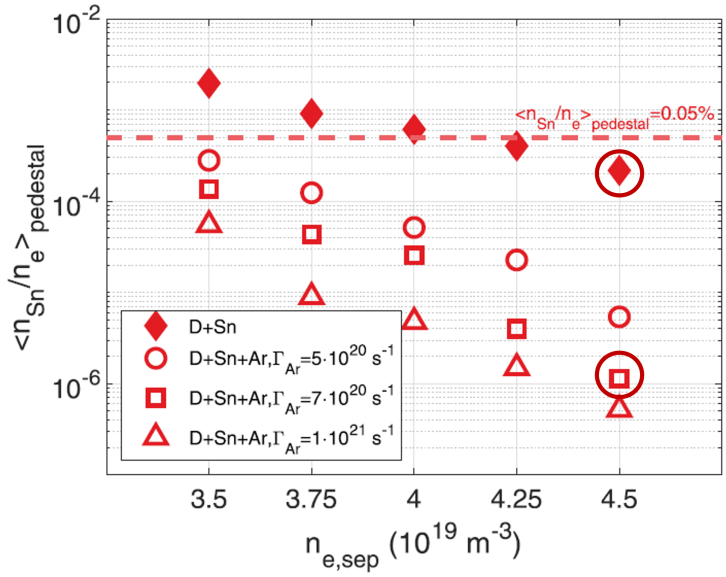

Figure 5.13: Plot representing different scenarios of Tin concentration taken into consideration in the work of [35]. The two cases under study are the ones highlighted in red circles.

- **Case 1** - $n_{Sn} = 3.45 \cdot 10^{-3}$ $[\frac{part}{m^3}]$

The following table 5.3 represents the usual engineering parameters accordingly to the ones previously shown for the Lithium case.

Case 1	
$\langle P_{fus} \rangle$	772 $[MW]$
$\langle C_Z \rangle$	0.01%
$\langle Z_{eff} \rangle$	1.2 [-]
$\langle T_e \rangle$	15 [keV]
$\langle T_i \rangle$	10 [keV]
$\langle n_{Li} \rangle$	$0.6 \cdot 10^{16}[\frac{part}{m^3}]$
$\langle n_e \rangle$	$7 \cdot 10^{19}[\frac{part}{m^3}]$
$\langle n_i \rangle$	$7 \cdot 10^{19}[\frac{part}{m^3}]$

Table 5.3: Table of interesting engineering values corresponding to the simulation with a source of Tin equal to $n_{Sn} = 3.45 \cdot 10^{16}[\frac{part}{m^3}]$

Looking at the values in the table 5.3, it is possible to verify that the fusion power is still not enough to fulfill the requirement of the reference scenario, due to the decrease of electron and ion temperatures with respect to the initial condition. By the way, the concentration of Tin $\langle C_Z \rangle$ is not overcoming the maximum value, hence the reason for the decrease of the fusion power should be addressed to the radiated power. To reinforce this thesis, values of electrons and ions average densities can be used: they are equal meaning that the accumulation of impurity is not enough to affect visibly the quasi-neutrality condition.

Focusing on the radial profiles of different parameters, the effects explained in the upper paragraph can be better visualized.

In figure 5.14, main plasma temperatures and powers are reported. The interesting effect is the very high values of radiated power at the edge of the core, where Tin is accumulated, as will be seen in figure 5.15. It is also possible to recognize that in the outer region, the main component of the total radiated power is indeed the one of the impurity, comprising both line and Bremsstrahlung radiation. For the case of Tin, in the range of temperature of the edge plasma, the contribution of line radiation and Bremsstrahlung are similar, since the heavy atom ($Z = 50$) of Tin has still enough electrons to be excited, but also the temperature promotes Bremsstrahlung radiation (see fig. 3.9).

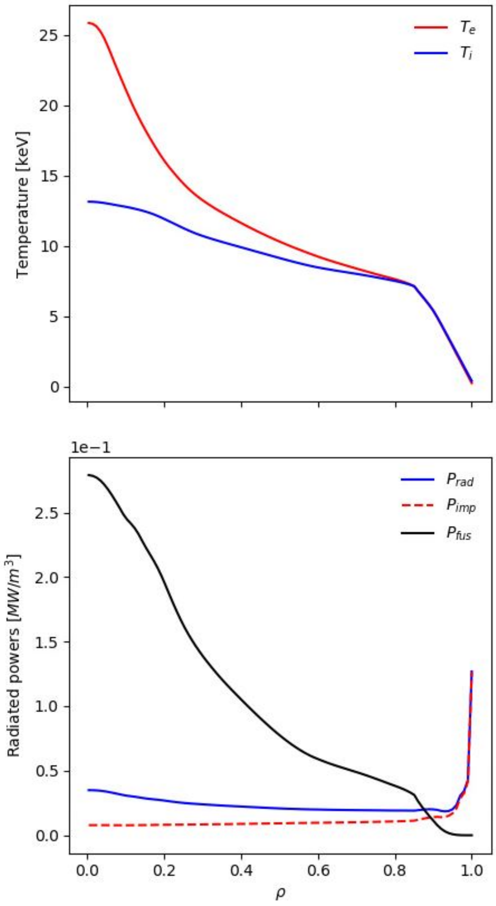

Figure 5.14: The figure represents the temperature profiles of the main plasma and the fusion and radiated power.

Having a look at the main plasma and impurity density profile, it is possible to recognize the absence of dilution since the electrons and ions shape are almost aligned, and the accumulation of the impurity at the edge.

This effect is the intended one since in this way the radiative losses are located at the edge of the plasma not affecting that much the core power. This behavior is explained by the shape of the total transport coefficients which are almost always positive and being the diffusive one way much bigger than the convective, as can be seen in figure 5.16.

For completeness, also the main plasma density and particle transport coefficient are shown 5.17, explaining the very small variations with respect to the initial values with the low values of diffusive and transport coefficients.

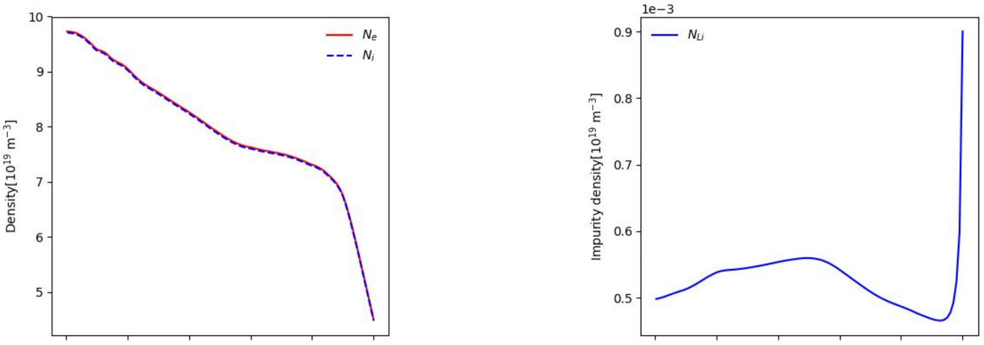

Figure 5.15: Radial profiles of main plasma and impurity density distribution

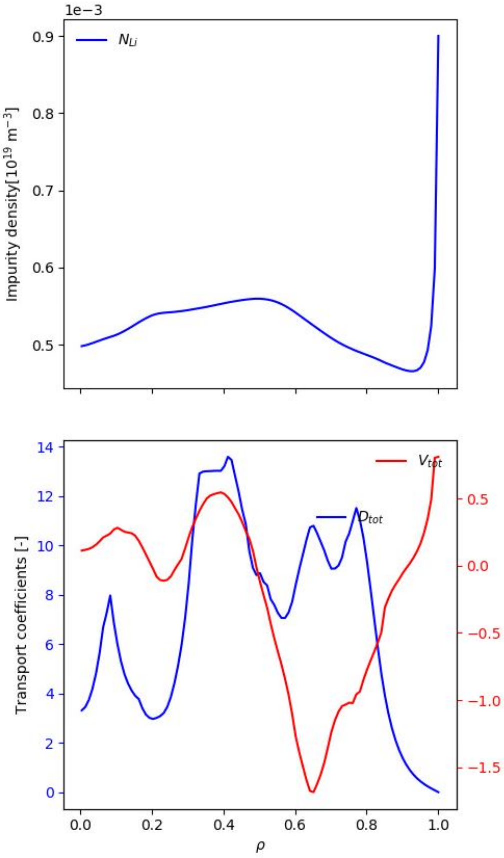

Figure 5.16: Radial profiles of Tin in the upper graph and correspondent total diffusive and convective coefficients in the bottom one.

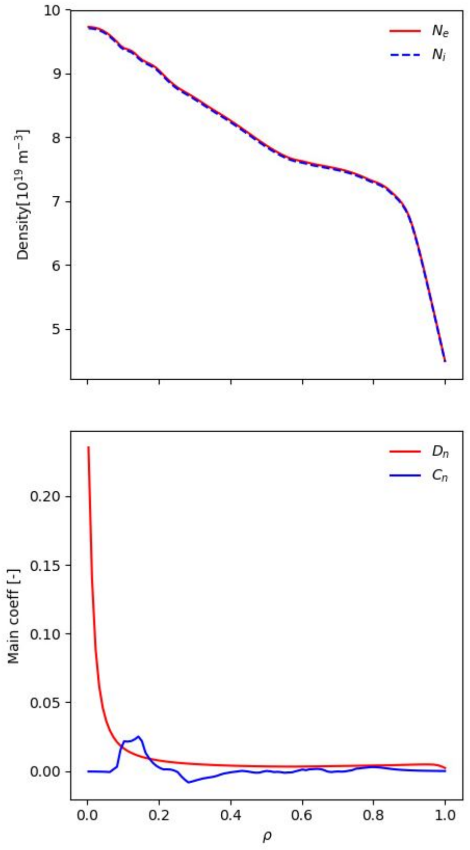

Figure 5.17: Radial profiles of main plasma density and correspondent particle transport coefficients.

- **Case 2** - $n_{Sn} = 4.5 \cdot 10^{13}$ $[\frac{part}{m^3}]$

  The second scenario under consideration for Tin represents some interesting effects. As in the other cases, the main engineering average parameters are represented.

  From the table 5.4, it is possible to recognize the very low value of impurity abundance C_Z, way below the maximum value depicted in figure 5.13. Indeed, fusion power is again very similar to the reference case. Actually, it gets a higher value, but this value, which could seem inconsistent, has to be seen as the resulting effect of fluctuation on transport coefficients and other numerical issues, more than a systematic result of the simulation, even if at convergence.

  Going to analyze the radial distribution of impurities, figure 5.18 shows

Case 2	
$\langle P_{fus} \rangle$	$841\ [MW]$
$\langle C_Z \rangle$	0.002%
$\langle Z_{eff} \rangle$	1.01 [-]
$\langle T_e \rangle$	13 [keV]
$\langle T_i \rangle$	10 [keV]
$\langle n_{Li} \rangle$	$0.5 \cdot 10^{15}[\frac{part}{m^3}]$
$\langle n_e \rangle$	$7 \cdot 10^{19}[\frac{part}{m^3}]$
$\langle n_i \rangle$	$7 \cdot 10^{19}[\frac{part}{m^3}]$

Table 5.4: Table of interesting engineering values corresponding to the simulation with a source of Tin equal to $n_{Sn} = 4.5 \cdot 10^{13}[\frac{part}{m^3}]$

an accumulation of impurity in the central region core, coherently to what transport coefficients describe, having the convective transport coefficient strong negative values.

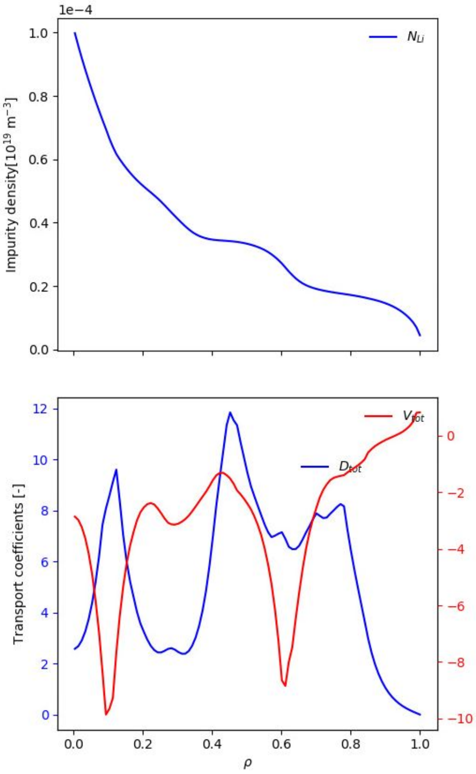

Figure 5.18: Radial profiles of Tin distribution in the upper graph and correspondent total diffusive and convective coefficients in the bottom one.

Consistently, the accumulation of particles in the central region led to not having any more radiation on the edge as in case 1, where in turn, the magnitude of radiation was higher. This can be explained by remembering the shape of the radiative cooling rate for Tin (fig 3.9). In fact, in the edge region, the temperature in the plasma is lower, and consequently, the rate of radiation increases.

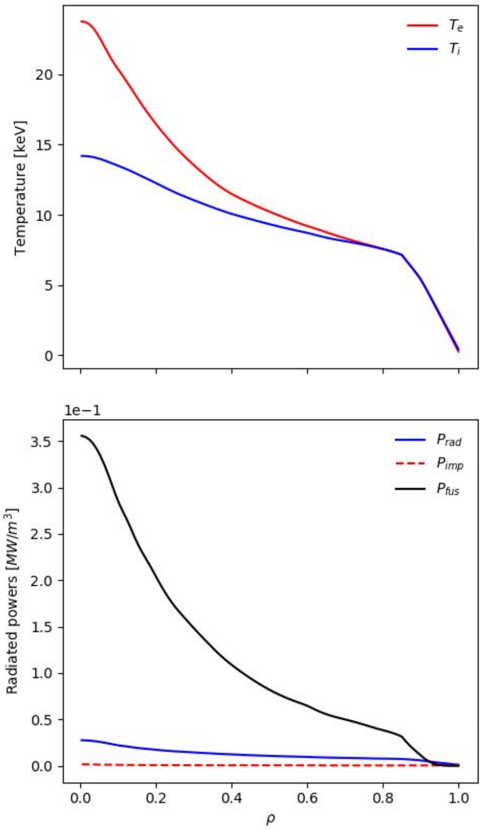

Figure 5.19: Radial profiles of main plasma temperature on the top graph and radiated and fusion power on the bottom graph.

For completeness, also the profile of ions and electrons density are reported in 5.20, together with the correspondent transport coefficients, which, with their very low value, describe coherently the upper profiles.

In conclusion to this section, it can be assessed that employing a very low source of Tin as in the second case (which in practice may be achieved via, e.g., Argon seeding), does not significantly affect that much the fusion power production with respect to a reference scenario without impurities, even with a core accumulation.

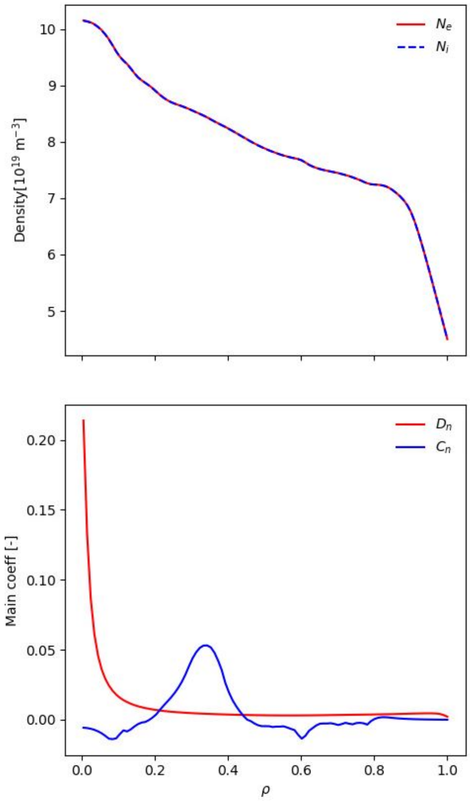

Figure 5.20: Radial profiles of main plasma temperature on the top graph and radiated and fusion power on the bottom graph.

5.2.4 Comparison between Lithium and Tin

Summarizing the main results obtained for the two impurities analyzed, some conclusions can be drawn.
It has been possible to verify that the harmful effects on the power balance of Lithium are due to the dilution, whereas Tin, with its very high radiative cooling rate, radiates very much in the core leading to an important decrease in fusion power.

On average it is possible to depict by looking at figure 5.21 that the radiated power of Lithium is lower with respect to Tin, as expected, even if the effects on fusion power and temperature are comparable, due to the different phenomena influencing the effects just explained.

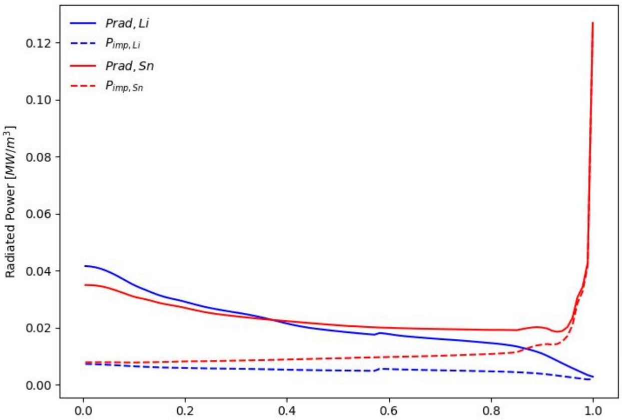

Figure 5.21: Radial profiles of total and impurity radiated power of Lithium and Tin, respectively in red and in blue, for the case of high impurity source.

The different accumulations of Lithium and Tin in the outer or inner side of the core are explained by the correspondent transport coefficients, considering the comments done on the effects of convective coefficients that require further improvements. In general, it is possible to see how the Lithium is accumulating always more on the inner side than on the outer, differently from the Tin case, which instead tends to accumulate in the central or in the outer region depending on the source value. Comparison between the two impurities at higher and lower values of the correspondent source is shown in figure 5.22, to depict the difference between the two impurities, of course, very big due to the high discrepancies of the boundary conditions, which are in turn consistent with the results from SOL-target calculations.

Electrons and ions and temperatures remain almost very similar to the reference case, differently from the fusion power, which instead varies from case to case, and a summary is presented in figure 5.23

Here, it can be seen that in any scenario with impurities, the fusion power density at the center of the core is decreased with respect to the reference case, as expected. Moreover, for the second case of both Lithium and Tin, depicted by the dashed lines, values are higher with respect to the corresponding continuum line and nearer to the reference scenario case.

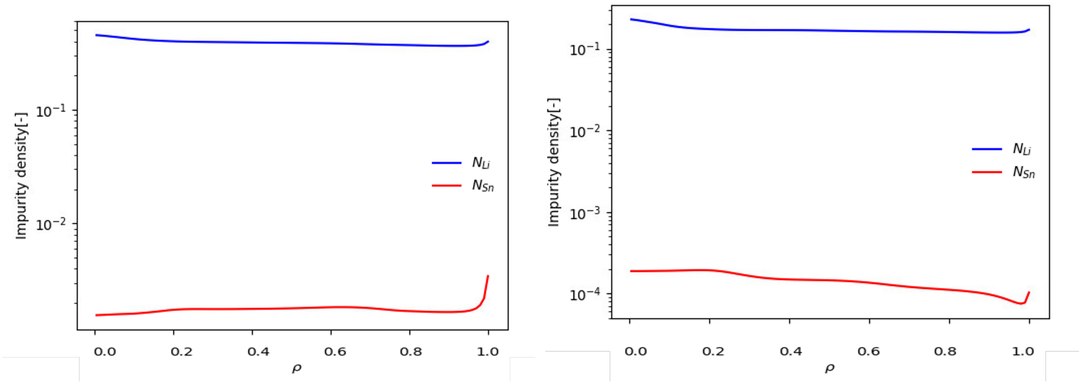

Figure 5.22: Radial profiles of Lithium and Tin impurity accumulation for the corresponding case with a higher source on the right-hand graph and with a lower source on the left-hand side.

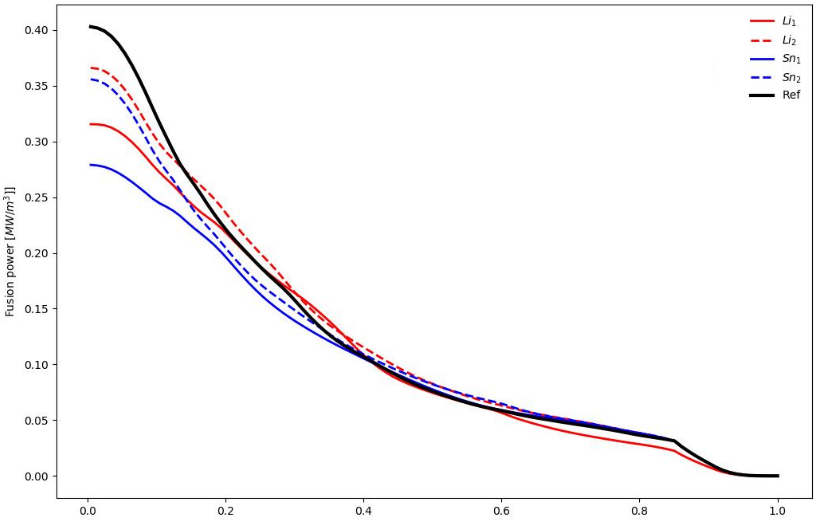

Figure 5.23: Comparison of resulting fusion power rates for the reference scenario in black, for the two cases of Lithium in red, and for the two cases of Tin in blue.

Chapter 6

Conclusions and future work

The comparison between the usage of Lithium or Tin as liquid metals in the divertor of the EU-DEMO Tokamak, in terms of their effect on the core plasma, has been qualitatively performed. The direct, one-way coupling between the output of SOLPS-ITER simulations and the core ones, performed with the ASTRA code, has been implemented, giving reasonable preliminary results.
In particular, the core transport modeling has been studied, focusing on the effects of the accumulation of impurities and correspondent radiated powers, in order to assess the feasibility of LMDs in terms of the power exhaust issue.
The main conclusion that can be drawn from the results of the comparison between the two impurity species is that a sufficient reduction of the source term for each of the impurities, which can be obtained for instance by seeding Ar in the SOL, results in affecting very low the fusion power, getting values very near to the reference case. Lithium is anyway producing dilution in the core plasma, even when a lower amount reaches the core, which is an undesired feature. Consequently, results here presented suggest that Tin is a more promising option for an LMD, at least from the core plasma point of view. Indeed, simulations with Tin seem to indicate that the resulting radiation, which is concentrated in the edge of the core region (due to both the accumulation of impurities and to the larger value of the radiation rate coefficient), may even be beneficial for the overall performance of the reactor - a conclusion which however needs to be supported by more detailed future studies.

From this thesis work, future improvements can be performed, first of all starting with the optimization of simulations.
The reason behind the small values of fusion power produced in the reference scenario and the correspondent main plasma temperatures with respect to what is expected for the EU-DEMO reactor producing 2 GW of fusion power has to be deeply analyzed and explained. This can be done starting from the study of heat transport coefficients and of other potential losses that could influence the decrease

of ions' and electrons' temperature.
Moreover, some instabilities have been encountered in the evaluation of turbulent transport coefficients by the TGLF code. The appropriate focus on this problem must be done, to assess the validity of the density and temperature distribution calculated.

For what concern the improvements that can be done, first of all, the coupling between the ASTRA and STRAHL code has to be completed. Yet, it does exist a coupling between the two codes, that anyway did not seem to give reliable results for the scenario analyzed in this thesis. More effort should be done in building a better coupling, avoiding numerical inconsistency, and getting reasonable results. This will allow accounting for the charge-state-wise impurity transport, thus relieving the coronal equilibrium assumption.
After that, an analysis of the effects arising from the different positioning of the boundary between the core and the SOL (the *separatrix*), can be performed, also studying the phenomena in the pedestal region.
Finally, once the core simulations are optimized and improved, the coupling in the inverse direction can be done, by providing input values to the SOLPS-ITER code, aiming to reach an iterative model for the integrated description of the whole target-SOL-core system.

Appendix A

Formulas for radiated power of Lithium and Tin

A.1 Lithium

- **Radiative cooling rate function**

```
! PRLIT [MW*m#3] Lithium radiation power
!       A.A. Mavrin, J. Fusion Energy 36
!       (Bray E. 16-11-2022)
!       Usage: PE=...-PRLIT*NE*NIZ1

   T=TE(J)*1000
   Z=LOG10(T)
   IF(T.LT.7..AND.T.GE.1.) then
   Y=-3.5752E1-1.6780*Z-6.1560*Z**2+1.1009E1*Z**3
   else if(T.LT.30..AND.T.GE.7.) then
   Y=-3.1170E1-1.6918E1*Z+2.0492E1*Z**2-7.0035*Z**3
   else if (T.LT.60..AND.T.GE.30.) then
   Y=-3.6558E1+9.4272*Z-8.1056*Z**2+1.9427*Z**3
   else if(T.LT.100..AND.T.GE.60.) then
   Y=-3.0560E1-2.4680*Z-2.8659E-1*Z**2+2.3898E-1*Z**3
   else if(T.LT.1000..AND.T.GE.100.) then
   Y=-3.0040E1-4.2963*Z+1.1569*Z**2-9.1510E-2*Z**3
   else if (T.LT.10000..AND.T.GE.1000.) then
   Y=-3.4199E1-8.5686E-1*Z+2.4968E-1*Z**2-1.7230E-2*Z**3
   else
   Y = -34.7959
```

```
   end if
   PRLIT = (10**Y)*1.e+32
```

- **Average charge**

```
! ZILIT [ ]: Average Li charge
! T [eV] Electron temperature
!      A.A. Mavrin, J. Fusion Energy 36
!      (Bray E. 16-11-2022)
!
T=TE(J)*1000
Z=LOG10(T)
       IF (T.LT.1)  then
       Y=0.
       else if(T.LT.7.AND.T.GE.1)    then
       Y=-1.0100E-3+2.7249E-1*Z-1.2369*Z**2+1.3026*Z**3
       else if(T.LT.30..AND.T.GE.7.) then
       Y=-2.0635+4.3288*Z-2.3837*Z**2+4.1307E-1*Z**3
       else if (T.LT.60..AND.T.GE.30.)  then
       Y=-1.0637+2.6510*Z-1.5162*Z**2+2.8809E-1*Z**3
       else if(T.LT.100..AND.T.GE.60.) then
       Y=-4.0067E-1+1.4848*Z-8.3674E-1*Z**2+1.5698E-1*Z**3
       else if(T.LT.1000..AND.T.GE.100.)   then
       Y=3.7673E-1+1.3675E-1*Z-6.1300E-2*Z**2+9.0100E-3*Z**3
       else IF(T.LT.10000..AND.T.GE.1000.) then
       Y=4.7538E-1+2.8900E-3*Z-1.1900E-3*Z**2+1.4464E-4*Z**3
       else
       Y=0.4771212547
       end if
       ZILIT = 10**Y
```

A.2 Tin

- **Radiative cooling rate function**

```
! PRTIN [MW*m#3] Lithium radiation power
!      A.A. Mavrin, J. Fusion Energy 36
!      (Bray E. 16-11-2022)
!      Usage: PE=...-PRTIN*NE*NIZ1
```

```
   T=TE(J)*1000
   Z =LOG10(T)
  IF(T.ge.100 .and. T .lt. 300)then
Y=6.29800501254456e-02 * Z**3 &
-2.28650242066325e+00 * Z**2 &
+ 8.90825634273927e+00 * Z**1 &
-3.95660535055000e+01 * Z**0
else IF(T.ge.300 .and. T .lt. 1000)then
Y=-3.27990411489566e+00 * Z**3 &
+ 2.69605680489987e+01 * Z**2 &
-7.43284074746929e+01 * Z**1 &
+ 3.79697102308800e+01 * Z**0
else IF(T.ge.1000 .and. T .lt. 2000)then
Y=-1.75754559836462e+01 * Z**3 &
+ 1.63262796356844e+02 * Z**2 &
-5.05337664675811e+02 * Z**1 &
+ 4.90274527597888e+02 * Z**0
else IF(T.ge.2000 .and. T .lt. 5000)then
Y=1.92654668633744e+00 * Z**3 &
-1.85489974274020e+01 * Z**2 &
+ 5.81529546308372e+01 * Z**1 &
-9.01508074163460e+01 * Z**0
else IF(T.ge.5000 .and. T .lt. 10000)then
Y=1.49264497067756e+01 * Z**3 &
-1.73847732754050e+02 * Z**2 &
+ 6.73491741451911e+02 * Z**1 &
-8.99360780192436e+02 * Z**0
else
Y=-9.68479196520852e-01 * Z**3 &
+ 1.33337615299491e+01 * Z**2 &
-6.10275887439805e+01 * Z**1 &
+ 6.10843015892650e+01 * Z**0
end if
   PRTIN = (10**Y)*1e+32 !account for Astra units
```

- **Average charge**

```
! ZITIN [MW*m#3] Lithium radiation power
!      A.A. Mavrin, J. Fusion Energy 36
!      (Bray E. 4/07/2023)
```

```
T=TE(J)*1000
Z = LOG10(T)
IF(T.ge.100 .and. T .lt. 300)then
Y=-1.74287118071950e-01 * Z**3 &
+ 1.54636650598728e+00 * Z**2 &
-3.99141529108946e+00 * Z**1 &
+ 4.33147417838939e+00 * Z**0
else IF(T.ge.300 .and. T .lt. 1000)then
Y=1.00244293446694e+00 * Z**3 &
-7.97732921344918e+00 * Z**2 &
+ 2.13382972994841e+01 * Z**1 &
-1.78615834244534e+01 * Z**0
else IF(T.ge.1000 .and. T .lt. 2000)then
Y=3.42895052030529e-01 * Z**3 &
-3.06822566369654e+00 * Z**2 &
+ 9.53786318906057e+00 * Z**1 &
-8.83692882480517e+00 * Z**0
else IF(T.ge.2000 .and. T .lt. 5000)then
Y=4.81585016923541e-01 * Z**3 &
-5.25915388459379e+00 * Z**2 &
+ 1.92606216460337e+01 * Z**1 &
-2.20499427661916e+01 * Z**0
else IF(T.ge.5000 .and. T .lt. 10000)then
Y=-2.08321206186342e+00 * Z**3 &
+ 2.39727274395118e+01 * Z**2 &
-9.17468909033947e+01 * Z**1 &
+ 1.18408176981176e+02 * Z**0
else
Y=9.91829921918504e-02 * Z**3 &
-1.32853805480940e+00 * Z**2 &
+ 5.94848074638099e+00 * Z**1 &
-7.22498252575176e+00 * Z**0
end if
ZITIN = 10**Y
```

Bibliography

[1] Jeffrey P. Freidberg. *Plasma physics and fusion energy / Jeffrey P. Freidberg.* eng. Cambridge: University Press, 2007. ISBN: 978-0-521-85107-7 (cit. on pp. 1, 16, 17, 19, 20, 27).

[2] Redazione. *Il Tokamak e la fusione magnetica, una fonte di energia alternativa?* it-IT. Jan. 2021. URL: `https://sciencecue.it/tokamak-fusione-magnetica-fonte-energia-alternativa/24425/` (visited on 06/09/2023) (cit. on p. 3).

[3] N. Mitchell et al. «Status of the ITER magnets». en. In: *Fusion Engineering and Design.* Proceeding of the 25th Symposium on Fusion Technology 84.2 (June 2009), pp. 113–121. ISSN: 0920-3796. DOI: `10.1016/j.fusengdes.2009.01.006`. URL: `https://www.sciencedirect.com/science/article/pii/S0920379609000301` (visited on 06/09/2023) (cit. on p. 3).

[4] J. Horacek, S. Lukes, J. Adamek, J. Havlicek, S. Entler, J. Seidl, J. Cavalier, J. Cikhardt, and V. Sedmidubsky. «Novel concept suppressing plasma heat pulses in a tokamak by fast divertor sweeping». en. In: *Scientific Reports* 12.1 (Oct. 2022). Number: 1 Publisher: Nature Publishing Group, p. 17013. ISSN: 2045-2322. DOI: `10.1038/s41598-022-18748-x`. URL: `https://www.nature.com/articles/s41598-022-18748-x` (visited on 06/09/2023) (cit. on p. 4).

[5] Emanuela Martelli, Fabio Giannetti, Gianfranco Caruso, Andrea Tarallo, Massimiliano Polidori, Luciana Barucca, and Alessandro Del Nevo. «Study of EU DEMO WCLL breeding blanket and primary heat transfer system integration». en. In: *Fusion Engineering and Design.* Special Issue: Proceedings of the 13th International Symposium on Fusion Nuclear Technology (ISFNT-13) 136 (Nov. 2018), pp. 828–833. ISSN: 0920-3796. DOI: `10.1016/j.fusengdes.2018.04.016`. URL: `https://www.sciencedirect.com/science/article/pii/S0920379618303041` (visited on 05/23/2023) (cit. on p. 4).

[6] F. Hernández, P. Pereslavtsev, Q. Kang, P. Norajitra, B. Kiss, G. Nádasi, and O. Bitz. «A new HCPB breeding blanket for the EU DEMO: Evolution, rationale and preliminary performances». en. In: *Fusion Engineering and Design.* Proceedings of the 29th Symposium on Fusion Technology (SOFT-29)

Prague, Czech Republic, September 5-9, 2016 124 (Nov. 2017), pp. 882–886. ISSN: 0920-3796. DOI: `10.1016/j.fusengdes.2017.02.008`. URL: `https://www.sciencedirect.com/science/article/pii/S0920379617300911` (visited on 05/23/2023) (cit. on p. 4).

[7] *International tokamak research*. en. URL: `http://www.iter.org/sci/tkmkresearch` (visited on 05/24/2023) (cit. on p. 5).

[8] *Roadmap*. en-US. URL: `https://euro-fusion.org/eurofusion/roadmap/` (visited on 05/24/2023) (cit. on p. 5).

[9] *What is ITER?* en. URL: `http://www.iter.org/proj/inafewlines` (visited on 05/24/2023) (cit. on p. 6).

[10] *Milestones around the world*. en. URL: `http://www.iter.org/sci/beyonditer` (visited on 05/24/2023) (cit. on p. 6).

[11] Sergio Ciattaglia, Gianfranco Federici, Luciana Barucca, Alessandro Lampasi, Simone Minucci, and Ivo Moscato. *The European DEMO fusion reactor: Design status and challenges from balance of plant point of view*. Pages: 6. June 2017. DOI: `10.1109/EEEIC.2017.7977853` (cit. on p. 6).

[12] *SPARC | Research | MIT Plasma Science and Fusion Center*. URL: `https://www.psfc.mit.edu/sparc` (visited on 06/26/2023) (cit. on p. 7).

[13] *Wendelstein 7-X*. en. URL: `https://www.ipp.mpg.de/w7x` (visited on 06/26/2023) (cit. on p. 7).

[14] *Proxima Fusion | Clean, Abundant, Safe Energy*. en. URL: `https://www.proximafusion.com/` (visited on 06/26/2023) (cit. on p. 7).

[15] Ivan Erofeev. «Advanced transport modelling in tokamak plasmas». PhD thesis. Technische Universität München, 2018. URL: `https://mediatum.ub.tum.de/1444870` (visited on 10/12/2022) (cit. on pp. 9, 23).

[16] *(6) (PDF) Basic Investigation of Turbulent Structures and Blobs of Relevance for Magnetic Fusion Plasmas*. URL: `https://www.researchgate.net/publication/259571717_Basic_Investigation_of_Turbulent_Structures_and_Blobs_of_Relevance_for_Magnetic_Fusion_Plasmas/figures?lo=1&utm_source=google&utm_medium=organic` (visited on 05/25/2023) (cit. on p. 9).

[17] *The divertor*. en. URL: `http://www.iter.org/mach/divertor` (visited on 05/25/2023) (cit. on p. 11).

[18] M. Turnyanskiy et al. «European roadmap to the realization of fusion energy: Mission for solution on heat-exhaust systems». en. In: *Fusion Engineering and Design* 96-97 (Oct. 2015), pp. 361–364. ISSN: 09203796. DOI: `10.1016/j.fusengdes.2015.04.041`. URL: `https://linkinghub.elsevier.com/retrieve/pii/S0920379615002707` (visited on 06/08/2023) (cit. on p. 11).

[19] *ITER ... and then what?* en. URL: `http://www.iter.org/mag/3/22` (visited on 06/08/2023) (cit. on p. 11).

[20] S. Roccella, G. Dose, R. de Luca, M. Iafrati, A. Mancini, and G. Mazzitelli. «CPS Based Liquid Metal Divertor Target for EU-DEMO». en. In: *Journal of Fusion Energy* 39.6 (Dec. 2020), pp. 462–468. ISSN: 1572-9591. DOI: `10.1007/s10894-020-00263-4`. URL: `https://doi.org/10.1007/s10894-020-00263-4` (visited on 06/08/2023) (cit. on pp. 11, 12).

[21] T. W. Morgan, P. Rindt, G. G. van Eden, V. Kvon, M. A. Jaworksi, and N. J. Lopes Cardozo. «Liquid metals as a divertor plasma-facing material explored using the Pilot-PSI and Magnum-PSI linear devices». en. In: *Plasma Physics and Controlled Fusion* 60.1 (Oct. 2017). Publisher: IOP Publishing, p. 014025. ISSN: 0741-3335. DOI: `10.1088/1361-6587/aa86cd`. URL: `https://dx.doi.org/10.1088/1361-6587/aa86cd` (visited on 06/08/2023) (cit. on p. 13).

[22] Per Helander. *Collisional transport in magnetized plasmas / Per Helander, Dieter J. Sigmar.* eng. Cambridge monographs on plasma physics 4. Cambridge ; Cambridge University Press, 2002. ISBN: 978-0-521-80798-2 (cit. on pp. 16, 21).

[23] Michael R. Hardman. *Hardman - Culham Plasma Physics Summer School 2022*. URL: `https://drive.google.com/drive/u/0/folders/1XfEHCbm6FzevFxt45JBPPZ9iNTBiD-jA?direction=a` (visited on 10/12/2022) (cit. on pp. 21, 22).

[24] Daniel Fajardo, Clemente Angioni, Patrick Maget, and Pierre Manas. «Analytical model for collisional impurity transport in tokamaks at arbitrary collisionality». In: *Plasma Physics and Controlled Fusion* 64 (Mar. 2022). DOI: `10.1088/1361-6587/ac5b4d` (cit. on p. 25).

[25] Clemente Angioni. *Phys. Rev. Lett. 96, 095003 (2006) - Direction of Impurity Pinch and Auxiliary Heating in Tokamak Plasmas*. URL: `https://journals.aps.org/prl/abstract/10.1103/PhysRevLett.96.095003` (visited on 06/23/2023) (cit. on p. 25).

[26] A. A. Mavrin. «Radiative Cooling Rates for Low-Z Impurities in Non-coronal Equilibrium State». en. In: *Journal of Fusion Energy* 36.4 (Oct. 2017), pp. 161–172. ISSN: 1572-9591. DOI: `10.1007/s10894-017-0136-z`. URL: `https://doi.org/10.1007/s10894-017-0136-z` (visited on 11/18/2022) (cit. on p. 25).

[27] Francesco Sciortino. *Aurora: a modern toolbox for impurity transport, neutrals and radiation modeling*. original-date: 2020-09-20T01:56:23Z. May 2023. URL: `https://github.com/fsciortino/Aurora` (visited on 07/05/2023) (cit. on p. 27).

[28] G V Pereverzev and P N Yushmanov. «ASTRA Automated System for TRansport Analysis». en. In: () (cit. on pp. 29–31).

[29] Ralph Dux. *STRAHL User Manual.* Sept. 2006. URL: `https://piscope1.psfc.mit.edu/images/f/f8/IPP_10_30.pdf` (cit. on p. 32).

[30] G. M. Staebler, J. E. Kinsey, and R. E. Waltz. «A theory-based transport model with comprehensive physicsa)». In: *Physics of Plasmas* 14.5 (May 2007), p. 055909. ISSN: 1070-664X. DOI: `10.1063/1.2436852`. URL: `https://doi.org/10.1063/1.2436852` (visited on 06/28/2023) (cit. on p. 33).

[31] W Herr. «Introduction to Landau Damping». en. In: (2014). Publisher: CERN. DOI: `10.5170/CERN-2014-009.377`. URL: `https://cds.cern.ch/record/1982428` (visited on 06/28/2023) (cit. on p. 33).

[32] *NCLASS_PT Help.* URL: `https://w3.pppl.gov/ntcc/NCLASS/readme_nclass_pt.html` (visited on 06/28/2023) (cit. on p. 34).

[33] Elena Tonello. *Numerical investigation of nuclear fusion relevant plasmas in linear devices through the SOLPS-ITER code.* URL: `http://hdl.handle.net/10589/145957` (cit. on p. 34).

[34] *H-mode: This discovery made ITER possible.* en. URL: `https://www.ipp.mpg.de/5280411/05_22` (visited on 06/28/2023) (cit. on p. 35).

[35] Giuseppe Francesco Nallo. *Modelling liquid metals for nuclear fusion and fission reactors.* URL: `https://hdl.handle.net/11583/2928622` (cit. on pp. 38, 44, 48, 54, 55).

[36] *OPEN-ADAS.* URL: `https://open.adas.ac.uk/` (visited on 07/07/2023) (cit. on p. 39).

[37] M. Siccinio, J. P. Graves, R. Kembleton, H. Lux, F. Maviglia, A. W. Morris, J. Morris, and H. Zohm. «Development of the plasma scenario for EU-DEMO: Status and plans». en. In: *Fusion Engineering and Design* 176 (Mar. 2022), p. 113047. ISSN: 0920-3796. DOI: `10.1016/j.fusengdes.2022.113047`. URL: `https://www.sciencedirect.com/science/article/pii/S0920379622000473` (visited on 07/05/2023) (cit. on pp. 41, 46).

[38] M. Poradziński, I. Ivanova-Stanik, G. Pełka, and R. Zagórski. «Integrated core-SOL-divertor modelling for DEMO with tin divertor». en. In: *Fusion Engineering and Design* 124 (Nov. 2017), pp. 248–251. ISSN: 09203796. DOI: `10.1016/j.fusengdes.2017.04.131`. URL: `https://linkinghub.elsevier.com/retrieve/pii/S0920379617305343` (visited on 07/08/2023) (cit. on pp. 47, 53, 54).